THE MILKY WAY TOMOGRAPHY WITH SDSS: III. STELLAR KINEMATICS

NICHOLAS BOND[3], ŽELJKO IVEZIĆ[1], BRANIMIR SESAR[1], MARIO JURIĆ[2], JEFFREY A. MUNN[20], ADAM KOWALSKI[1], SARAH LOEBMAN[1], ROK ROŠKAR[1], TIMOTHY C. BEERS[7], JULIANNE DALCANTON[1], CONSTANCE M. ROCKOSI[4], BRIAN YANNY[5], HEIDI J. NEWBERG[6], CARLOS ALLENDE PRIETO[8], RON WILHELM[9], YOUNG SUN LEE[7], THIRUPATHI SIVARANI[7], JOHN E. NORRIS[10], CORYN A.L. BAILER-JONES[11], PAOLA RE FIORENTIN[11,12], DAVID SCHLEGEL[13], ALAN UOMOTO[14], ROBERT H. LUPTON[3], GILLIAN R. KNAPP[3], JAMES E. GUNN[3], KEVIN R. COVEY[15], J. ALLYN SMITH[16], GAJUS MIKNAITIS[5], MAMORU DOI,[17], MASAYUKI TANAKA[18], MASATAKA FUKUGITA[19], STEVE KENT[5], DOUGLAS FINKBEINER[15], TOM R. QUINN[1], SUZANNE HAWLEY[1], SCOTT ANDERSON[1], FUREA KIUCHI[1], ALEX CHEN[1], JAMES BUSHONG[1], HARKIRAT SOHI[1], DARYL HAGGARD[1], AMY KIMBALL[1], ROSALIE MCGURK[1], JOHN BARENTINE[21], HOWARD BREWINGTON[21], MIKE HARVANEK[21], SCOTT KLEINMAN[21], JUREK KRZESINSKI[21], DAN LONG[21], ATSUKO NITTA[21], STEPHANIE SNEDDEN[21], BRIAN LEE[13], JEFFREY R. PIER[20], HUGH HARRIS[20], JONATHAN BRINKMANN[21], DONALD P. SCHNEIDER[22], DONALD G. YORK[23]

Draft version April 16, 2009

ABSTRACT

We analyze the Milky Way kinematics using a sample of 30 million main-sequence stars with proper motion measurements derived from SDSS and POSS astrometry. For $\sim$100,000 of these stars radial velocity measurements are also available from the SDSS spectroscopic survey. Distances to stars are determined using a photometric parallax relation, and photometric metallicity estimates are also available for F/G stars. These stars sample a distance range from 100 pc to 10 kpc, at high galactic latitudes ($|b| >$30, about 10,000 deg^2, with a much smaller area in the southern galactic hemispere), and allow a detailed and robust determination of the velocity field as a function of location and metallicity. We find that in the region defined by 1 kpc $<$ Z $<$ 5 kpc and 3 kpc $<$ R $<$ 13 kpc, the rotational velocity and all three components of velocity dispersion for disk stars smoothly increase with distance from the galactic plane. In contrast, the velocity ellipsoid for halo stars is aligned with spherical coordinate system and spatially invariant within the probed volume. The velocity distribution of nearby (Z $<$ 1 kpc) red stars (K/M) is complex and cannot be described by standard Schwarzschild ellipsoid. For stars in a distance-limited subsample equivalent to HIPPARCOS sample ($<$100 pc), we detect multimodal distribution consistent with HIPPARCOS results and similar to Eggen's moving groups. This strong non-gaussianity significantly affects the measurements of velocity ellipsoid tilt and vertex deviation when using the Schwarzschild approximation. We develop and test a relatively simple descriptive model for the overall kinematic behavior that captures these features over most of the probed volume, and can be used to search for fine substructure in kinematic and metallicity space. We use this model to predict further improvements expected from Gaia and LSST.

Subject headings: methods: data analysis — stars: statistics — Galaxy: halo, kinematics and dynamics, stellar content, structure

[1] Department of Astronomy, University of Washington, Box 351580, Seattle, WA 98195

[2] Institute for Advanced Study, 1 Einstein Drive, Princeton, NJ 08540

[3] Princeton University Observatory, Princeton, NJ 08544

[4] University of California–Santa Cruz, 1156 High St., Santa Cruz, CA 95060

[5] Fermi National Accelerator Laboratory, P.O. Box 500, Batavia, IL 60510

[6] Department of Physics, Applied Physics, and Astronomy, Rensselaer Polytechnic Institute, 110 8th St., Troy, NY 12180

[7] Dept. of Physics & Astronomy, CSCE: Center for the Study of Cosmic Evolution, and JINA: Joint Institute for Nuclear Astrophysics, Michigan State University, East Lansing, MI 48824, USA

[8] McDonald Observatory and Department of Astronomy, University of Texas, Austin, TX 78712

[9] Department of Physics, Texas Tech University, Box 41051, Lubbock, TX 79409

[10] Research School of Astronomy & Astrophysics, The Australian National University, Cotter Road, Weston, ACT 2611, Australia

[11] Max Planck Institut für Astronomie, Königstuhl 17, 69117 Heidelberg, Germany

[12] Department of Physics, University of Ljubljana, Jadranska 19, 1000 Ljubljana, Slovenia

[13] Lawrence Berkeley National Laboratory, One Cyclotron Road, MS 50R5032, Berkeley, CA, 94720

[14] Department of Physics and Astronomy, The John Hopkins University, 3701 San Martin Drive, Baltimore, MD 21218

[15] Harvard-Smithsonian Center for Astrophysics, 60 Garden Street, Cambridge, MA 02138

[16] Dept. of Physics & Astronomy, Austin Peay State University, Clarksville, TN 37044

[17] Institute of Astronomy, University of Tokyo, 2-21-1 Osawa, Mitaka, Tokyo 181-0015, Japan

[18] Dept. of Astronomy, Graduate School of Science, University of Tokyo, Hongo 7-3-1, Bunkyo-ku, Tokyo, 113-0033, Japan

[19] Institute for Cosmic Ray Research, University of Tokyo, Kashiwa, Chiba, Japan

[20] U.S. Naval Observatory, Flagstaff Station, P.O. Box 1149, Flagstaff, AZ 86002

[21] Apache Point Observatory, 2001 Apache Point Road, P.O. Box 59, Sunspot, NM 88349-0059

[22] Department of Astronomy and Astrophysics, The Pennsylvania State University, University Park, PA 16802

[23] University of Chicago, Astronomy & Astrophysics Center, 5640 S. Ellis Ave., Chicago, IL 60637

1. INTRODUCTION

The Milky Way is a complex and dynamical structure that is still being shaped by the infall (merging) of neighboring smaller galaxies. Since we are part of it, the Milky Way provides a unique opportunity to study a galaxy in great detail by measuring and analyzing the properties of a large number of individual stars. Most studies of the Milky Way structure can be described as investigations of the stellar distribution in the nine-dimensional space spanned by the three spatial coordinates, three velocity components, and three main stellar parameters (luminosity, effective temperature, and metallicity).

In this paper, and the first two papers of this series, we use data obtained by the Sloan Digital Sky Survey (York et al. 2000) to study in detail the distribution of tens of millions of stars in this multi-dimensional space. We studied stellar counts in Jurić et al. (2008, hereafter J08), and in Ivezić et al. (2008, I08) we extended our analysis to include metallicity distribution. Here we focus on kinematics and analyze an unprecedentedly large kinematic data set enabled by SDSS astrometric, photometric and spectroscopic surveys: the radial velocity sample includes XXX stars, and the proper motion sample includes XXX stars, with about XXX F/G stars in the latter sample for which photometric metallicity estimates are also available. These stars sample the distance range from ∼100 pc to ∼10 kpc, which represents a significant advance compared to the HIPPARCOS distance range of <100 pc (e.g., Dehnen & Binney 1998; Nordström et al. 2004). SDSS dataset offers for the first time an opportunity to study *in situ* the thin/thick disk and disk/halo boundaries over a significant fraction of the sky and using numerous main-sequence stars.

A common feature of the papers in this series is the use of photometric parallax relations, enabled by accurate SDSS multi-color measurements, to estimate distance to main-sequence stars. With these distances, accurate to ∼10-15%, the multi-dimensional stellar distribution can be mapped and analyzed without any additional assumptions. The main aim of this paper is to develop quantitative understanding of the large-scale kinematic behavior of disk and halo stars. From an observer's point of view, the goal is to measure and describe the radial velocity and proper motion distributions as functions of the position in, say, the r vs. $g - r$ color-magnitude diagram, and as functions of the position of the analyzed sample on the sky. From a theorist's point of view, we seek to quantify the behavior of the probability distribution function $p(v_R, v_\phi, v_Z | R, \phi, Z, [Fe/H])$, where (v_ϕ, v_R, v_Z) are the three velocity components in a cylindrical coordinate system, (R, ϕ, Z) describe the position of a star in the Galaxy, and $[Fe/H]$ is its metallicity ("|" means "given").

This a different approach than that taken by the most widely used "Besançon" Galaxy model (Robin et al. 2003, and references therein). Instead of attempting to generate model stellar distributions from "first principles" (such as initial mass function) and by requiring dynamical self-consistency, we simply seek to describe the observed distributions without imposing any additional constraints. Our approach thus makes maximum use of photometric parallax relations to dissect the Galaxy in multi-dimensional position-metallicity-velocity space. If these new voluminous data sets analyzed here can be described in terms of simple functions, then one can try to understand and model those simple abstractions, rather than full data set.

As discussed in detail by J08 and I08, disk and halo components have distinctive spatial and metallicity distributions, which can be well described using simple analytic models within the volume probed by SDSS (and outside regions with strong substructure, such as Sgr dwarf tidal stream and Monoceros stream). Here we develop analogous models that describe the velocity distributions of disk and halo stars. Some of detailed questions that we ask include: what are the limitations of the Schwarzschild's ellipsoidal approximation (a three-dimensional gaussian distribution) for describing velocity distribution? Given the increased distance range compared to older data sets, can we detect spatial variation of the best-fit Schwarzschild ellipsoid parameters, including its orientation? Does halo rotate on average? Is the kinematic difference between disk and halo stars as remarkable as the difference in their metallicity distributions? Do large spatial substructures, that are also traced in metallicity space, have distinctive kinematic behavior?

Of course, answers to some of these questions are known to some extent. For example, it has been known at least since the seminal paper by Eggen, Lynden-Bell & Sandage (1962) that high-metallicity disk stars move on nearly circular orbits, while low-metallicity halo stars move on very eccentric randomly oriented orbits. However, given the increase in the number of stars compared to previous work (orders of magnitude), increased distance limits, and accurate and diverse measurements obtained with the same facility, the previous results can be significantly improved and expanded.

The main sections of the paper include a description of the data and methodology (§2), analysis of proper motion sample (§3), analysis of a subsample with radial velocity measurements (§4), kinematic model testing (§5), and summary and discussion, including a comparison with prior results and other works based on SDSS data (§6).

Due to length, some additional aspects of our analysis are presented separately. A detailed analysis of two-dimensional radial vs. rotational velocity distribution ($v_R - v_\phi$) for nearby main-sequence M stars as a function of distance from the plane, Z, is presented by Kowalski et al. (in prep.). Using a sample of several million stars, they find that the $v_R - v_\phi$ distribution can be described by a sum of two Gaussians that have similar parameters as traditional thin and thick disk kinematics; however, they also obtained an intriguing result that the relative normalization of the two gaussian components does not vary by more than 0.05 as Z increases from ∼200 pc to ∼1.5 kpc (the counts profile from J08 predicts a change from 0.15:0.85 to 0.65:0.35). A comparison of SDSS metallicity and kinematic distributions with N-body models by Roškar et al. (2008) is presented in Loebman et al. (in prep; for initial results see Loebman et al. 2008); models indicate that the unexpected absence of velocity-metallicity correlation at the thin/thick disk boundary pointed out by I08 may be due to a combination of strong vertical age gradient and radial migration of stars.

2. DATA AND METHODOLOGY

The characteristics of SDSS imaging and spectroscopic data relevant for this work are described in detail in the first two papers in the series (J08, I08). Here we briefly summarize the photometric parallax and photometric metallicity methods, and then describe the proper motion data and their error analysis. The outline for the two subsequent analysis sections, and the subsample definitions, are described at the end of this section.

2.1. *Photometric Parallax Method*

The majority of stars in SDSS imaging catalogs are on main sequence (J08 and references therein) and, thanks to accurate multi-color photometry, it is possible to estimate their absolute magnitude from the measured colors. A maximum likelihood implementation of the photometric parallax method in SDSS photometric system was introduced and discussed in detail in J08. The method was further refined by I08 who calibrated its dependence on metallicity using data for a set of globular clusters. Sesar et al. (2008) used a large sample of candidate wide binary stars to show that the expected error distribution is mildly non-gaussian, with a root-mean-square (rms) scatter of ∼0.3 mag. They also quantified biases due to unresolved binary stars.

We estimate absolute magnitudes using expression (A7) from I08, which attempts to correct for age effects, and expression (A2) which accounts for the impact of metallicity. Based on globular cluster analysis by I08, probable systematic errors in absolute magnitudes determined using these relations are about about 0.1 mag, corresponding to systematic 5% distance errors (in addition to 10-15% random distance errors).

2.2. *Photometric Metallicity*

Stellar metallicity significantly affects the position of absolute magnitude vs. color sequence (a shift of ∼1 mag between the median halo metallicity of −1.5 and the median disk metallicity of −0.2). Since metallicity derived from SDSS spectroscopy is available only for a small fraction of all stars detected in SDSS imaging data and analyzed here, we adopt photometric metallicity method based on SDSS $u-g$ and $g-r$ colors and calibrated by I08 using SDSS spectroscopic metallicity.

The calibration of SDSS spectroscopic metallicity changed at the high-metallicity end after SDSS Data Release 6 used by I08. We re-calibrate their expressions, as described in Appendix: *here we use the new calibration given by eq.*A1. This expression is applicable to F/G stars with $0.2 < g-r < 0.6$. The photometric metallicity errors are discussed in detail in Appendix; approximately, they follow a gaussian distribution with a width of 0.26 dex. Of course, all systematic uncertainties in SDSS spectroscopic metallicity are inherited by photometric metallicity estimator. They are of the order 0.1 dex (Beers et al. 2006; Allende Prieto et al. 2006; Lee et al. 2007ab; Allende Prieto et al. 2007).

For stars with $g-r > 0.6$, we assume a constant metallicity of $[Fe/H] = −0.6$. This value is motivated by results on disk metallicity distribution presented in I08, and the fact that SDSS data are too shallow to include a large fraction of halo red stars. A slightly better method would be to use disk metallicity distribution from I08 to solve for best-fit distance iteratively. However, the distance differences between the two approaches are smaller than, or at most comparable to, other systematic errors.

2.3. *SDSS-POSS Proper Motion Catalog*

We take proper motion measurements from the Munn et al. (2004) catalog (distributed as a part of public SDSS data releases). This catalog is based on astrometric measurements from SDSS and a collection of Schmidt photographic surveys. Despite the sizable random and systematic astrometric errors in the Schmidt surveys, the combination of a long baseline (∼50 years for POSS-I survey), and a recalibration of the photographic data using positions of SDSS galaxies (see Munn et al. for details), result in median random proper motion errors (per component) of only ∼ 3 mas yr^{-1} for $r < 18$ and ∼ 5 mas yr^{-1} for $r < 20$ (the faint limit). Systematic errors are typically an order of magnitude smaller, as robustly determined using spectroscopically confirmed SDSS quasars (see below). At a distance of 1 kpc, a random error of 3 mas yr^{-1} corresponds to a velocity error of ∼15 km s^{-1}, which is comparable to the radial velocity accuracy delivered by the SDSS stellar spectroscopic survey. At a distance of 7 kpc, a random error of 3 mas yr^{-1} corresponds to a velocity error of 100 km s^{-1}, which still represents a usable measurement for large samples, given that systematic errors are much smaller (∼20 km s^{-1}at a distance of 7 kpc). Due to sufficiently small and well understood proper motion errors, together with a large distance limit and a large sample size (proper motion measurements are available for about XXX million stars with $r < 20$ from SDSS Data Release 7), this catalog represents an unprecedently powerful resource for studying the kinematics of the Milky Way stars.

We warn the reader that proper motion measurements publicly available prior to SDSS Data Release 7 are known to have significant systematic errors. Here we use a revised set of proper motion measurements (Munn et al. 2008), which are publicly available only since Data Release 7. In order to assess the error properties of this revised proper motion catalog, we use quasars, described next.

2.3.1. *Determination of Proper Motion Errors Using Quasars*

Quasars are sufficiently far away that their proper motions are negligible at the accuracy level considered here. The large number of spectroscopically confirmed SDSS quasars (Schneider et al. 2007), which were not used in the recalibration of POSS astrometry, can thus be used to derive robust independent estimates of, both random and systematic, proper motion errors. The distributions of proper motions for 54,811 quasars with $15 < r < 20$ have a standard deviation of ∼3.5 mas/yr for each component (determined from inter-quartile range), with medians differing from zero by less than 0.2 mas/yr. The standard deviation, which represents a measurement of random errors, is a function of apparent magnitude, and well summarized by the following empirical fit

$$\sigma_\mu = 2.7 + 2.0\,10^{0.4\,(r-20)}\,\mathrm{mas/yr} \qquad (1)$$

in the $15 < r < 20$ range. When the measurements of each proper motion component are normalized by σ_μ, the resulting distribution is essentially Gaussian, with only ∼1.4% of the sample deviating by more than 3 from zero. The correlation between the two components is negligible compared to the intrinsic scatter.

The median proper motions for the full quasar sample show that the systematic errors averaged over the whole observed sky region are at most 0.2 mas/yr. However, they can be larger by a factor of 2-3 in small sky patches, as illustrated in Figure A1. We find that the distribution of systematic proper motion errors in ∼100 deg^2 large patches has a width of ∼0.67 mas/yr (same for each component), or about twice as large as expected from purely statistical noise (per bin). As the figure shows, a few regions of the sky have coherent systematic errors at the level close to 1 mas/yr (e.g. the median μ_l towards $l \sim 270°$, or μ_b towards the inner Galaxy). Therefore, the interpretation of kinematics measured using proper motions towards these regions should be cautious.

The region with the largest systematic errors, ∼ 1 mas/yr for μ_l (the top region in the top left panel in Figure A1), is observed at low declination ($\delta \lesssim 10°$). The systematic deviation of quasar vector proper motions from zero is approximately parallel to the lines of constant right ascension ($\langle\mu_\alpha\rangle \sim 0$, and

$\langle \mu_\delta \rangle \sim -1$ mas/yr), which suggests that this effect could be caused by atmospheric refraction (due to spectral differences between quasars and galaxies used in the recalibration of POSS astrometry). Such an effect would be the strongest for observations obtained at high airmass, which increases for fields with low declinations (the POSS data were obtained at a latitude of $+33°$; the SDSS data have a median airmass of ~ 1.4). We find that the median quasar proper motion in the δ direction is well described by

$$\langle \mu_\delta \rangle = -0.72 + 0.019\,\delta \text{ mas/yr} \tag{2}$$

for $-5° < \delta < 30°$, and $\langle \mu_\delta \rangle \lesssim 0.2$ mas/yr for $\delta > 30°$.

The observed direction and the magnitude of this systematic offset (an astrometric displacement of up ~ 30 mas) are consistent with detailed studies of atmospheric dispersion effects for quasars (Kaczmarczik, Richards & Schlegel 2007). Therefore, it is possible that true systematic errors for stellar proper motions (whose spectral energy distributions differ less from galaxy spectral energy distributions than is the case for quasars) are smaller than implied by Figure A1. Nevertheless, we will conservatively adopt results based on quasars as independent estimates of systematic and random proper motion errors for stars analyzed in this work. In particular, we adopt 0.6 mas/yr as an estimate for typical systematic proper motion error. Such a small value is truly remarkable as it corresponds to an astrometric systematic error of only 30 mas (assuming 50 year long baseline).

A systematic error in proper motion of 0.6 mas/yr corresponds to a systematic velocity error of 3 km s^{-1} at 1 kpc, and ~ 20 km s^{-1} at 7 kpc. At the same time, systematic distance errors of $\sim 10\%$ (due to both intrinsic photometric parallax errors and systematic errors in metallicity) are responsible for a $\sim 10\%$ systematic velocity uncertainty. Hence, for a disk-like heliocentric tangential velocity of 20 km s^{-1}, proper motion systematics dominate at distances beyond ~ 1 kpc, and at distances beyond 7 kpc for a halo-like heliocentric tangential velocity of 200 km s^{-1}. At smaller distances, the dominant systematic tangential velocity error comes from systematic distance errors. It turns out that throughout most of the Galaxy volume analyzed in this work, the systematic distance errors are more important effect than systematic proper motion errors (though the latter display a coherent behavior as a function of position on the sky in certain directions).

The quasar sample has a much narrower color distribution than main sequence stars (96% of quasar sample satisfies $-0.2 < g-r < 0.6$), and provides a better estimate of systematic proper motion errors for blue than for red stars. Within the $-0.2 < g-r < 0.6$ color range, we find that the gradient of median proper motion is $\lesssim 0.1$ mas/yr/mag (per component). When the fit is extended to $g-r < 1.6$ (using a much smaller number of quasars), the gradient is still smaller than 0.5 mas/yr/mag. Hence, the color systematics are smaller than, or at most comparable to, proper motion systematics as a function of position on the sky.

In addition to their dependence on magnitude, the random proper motion errors also depend on the position on the sky, but the variation is much smaller than for systematic errors (see right panels in Figure A1). A region with the largest deviation ($170° < \alpha < 230°$ and $\delta < 10°$, corresponding to $300° < l < 330°$) has the distribution width for the proper motion component parallel to right ascension increased to 5 mas/yr, from 3-4 mas/yr for the rest of the sky (and for the other component).

2.4. *Comparison of Proper Motions with Independent Measurements*

Describe here the comparison with Majewski's and stripe 82 samples. Independent support for the above conclusions.

2.5. *Complexities Associated with Kinematic Analysis*

It is more difficult to analyze kinematic data than stellar counts and metallicity data, as done in the first two papers. While stellar counts in appropriately chosen volume elements are a scalar quantity, metallicity and velocity data represent distributions (probability densities). Furthermore, in the kinematic case there are three distributions, which can be, at least in principle, strongly correlated. Even for a perfect Gaussian velocity distribution (the Schwarzschild ellipsoid), there are still as many as six scalar functions to follow as a function of position in the Galaxy and metallicity. Another way to look at the same problem, more similar to analysis presented in Paper I, is that we are trying to count stars and constrain the distribution function in the 7-dimensional space spanned by three spatial coordinates, three velocity components and metallicity. Assuming rotational symmetry of the Galaxy, and that stars can be simply separated in low-metallicity and high-metallicity subsamples, this is still counting in a 5-dimensional space.

An added difficulty when analyzing kinematics is complex error behavior. Random errors for radial velocity measurements depend on magnitude, and thus distance, due to varying signal-to-noise ratio. When using proper motions, in addition to even stronger dependence of random velocity errors on distance, systematic errors are also a function of position on the sky, as discussed above. When radial velocity and proper motion measurements are analyzed simultaneously, the various systematic and random errors combine in a complex way and substantial care is needed when interpreting results.

2.6. *The Main Stellar Samples*

Given various complexities listed above, we chose to treat the large proper motion sample, and the much smaller spectroscopic sample separately. Motivated by metallicity distribution functions quantified by I08, we separately treat low-metallicity "halo" stars and high-metallicity "disk" stars. For both samples, we require $g-r < 0.6$ mandated by the validity region of the photometric metallicity estimator. In addition, we also discuss a sample of "red" stars with $g-r > 0.6$ (roughly, $g-i > 0.8$), which are dominated by nearby (<2 kpc) disk stars. These samples are selected from SDSS Data Release 7 using the following common criteria:

1. unique unresolved stationary sources: binary processing flags DEBLENDED_AS_MOVING, SATURATED, BLENDED, BRIGHT, and NODEBLEND must be false, and parameter nCHILD=0

2. the interstellar extinction in the r band below 0.3

3. $14.5 < r < 20$

4. available proper motion (XXX more details),

that yield XXX stars, and these specialized color criteria that select stars from the main stellar locus:

- Blue stars (XXX):

   1. $0.2 < (g-r) < 0.6$
   2. $0.7 < (u-g) < 2.0$ and $-0.25 < (g-r) - 0.5(u-g) < 0.05$

3. $-0.2 < 0.35(g-r) - (r-i) < 0.10$

- Red stars (XXX):

  1. $0.6 < (g-r) < 1.6$

  2. $-0.15 < -0.270\,r + 0.800\,i - 0.534\,z + 0.054 < 0.15$,

where the last condition is based on principal color definition in the $i-z$ vs. $r-i$ color-color diagram from Ivezić et al. (2004), and allows for 0.15 mag offset from the locus. During analysis, "blue" stars are often further split into XXX halo stars with $[Fe/H] < -1.1$ and YYY disk stars with $[Fe/H] > -0.9$, using *photometric* metallicity (see below for more details). Subsamples with intermediate metallicities include non-negligible fractions of both halo and disk stars.

For each sample, we extract subsamples with spectroscopic data. After an additional requirement to select main-sequence stars, $log(g) > 3$ (note that for the majority of stars with $g-r > 1.2$ $log(g)$ is not reliably determined by spectroscopic pipeline and values are set to -9.99; we assume that all stars with $g-r > 1.2$ are main-sequence stars), the final samples include 119,000 stars. They are split into subsamples of 73,000 blue $(0.2 < g-r < 0.6)$ stars and 46,000 red $(0.6 < g-r < 1.6)$ stars. When separating low- and high-metallicity stars with spectra, we use *spectroscopic* metallicity.

2.7. *Analysis Philosophy*

Such a large data set, that probes a large fraction of the Galaxy volume, and extends to a large distance limit, can be used to map stellar kinematics in great detail. It can also be used to obtain best-fit parameters of an appropriate kinematic model. However, it is not obvious what model (functional form) to chose without at least some preliminary analysis. Hence, we first discuss various projections of the multi-dimensional space spanned by positional coordinates, velocity and metallicity and obtain a number of constraints on the spatial variation of kinematics in the next two sections, and then synthesize all the constraints into a model described in § 5.

Separation (or classification) of halo and disk stars is an important aspect of this work. Reduced proper motion diagram is a standard tool to classify samples with kinematic information. Nevertheless, we choose not to use this tool for two main reasons. First, reliable separation can be obtained only for stars with significant motion (depending on projection of velocity vector and measurement errors) and the resulting samples have to be statistically corrected for missing stars. This correction requires the knowledge of the velocity distribution, which is the quantity we are trying to determine in the first place. Second, the vertical gradient of rotational velocity for disk stars makes the distinction between disk and halo stars blurred at several kpc from the plane (see Sesar et al. 2008 for a detailed discussion). Instead of reduced proper motion diagram, we use metallicity to separate blue stars into halo and disk subsamples. Results from I08 imply that red stars, for which metallicity is not available, are dominated by disk stars due to their smaller distance limit. A detailed analysis of the performance and tradeoffs between kinematic and metallicity based methods is presented in Bhardwaj et al. (in prep.).

We first analyze the proper motion sample and determine the dependence of the azimuthal and radial velocity distributions on position for halo and disk subsamples selected along the main meridian ($l = 0°$ and $l = 180°$). The spectroscopic sample is used in §4 to obtain constraints for the behavior of vertical velocity component, and to measure the velocity ellipsoid tilt. The resulting model is then compared to the full proper motion sample and radial velocity sample in §5.

2.8. *Coordinate Systems and Transformations*

Following J08 and I08, we use a *right-handed* Cartesian galactocentric coordinate system defined by the following set of coordinate transformations:

$$X = R_\odot - D\cos(l)\cos(b)$$
$$Y = -D\sin(l)\cos(b) \qquad (3)$$
$$Z = D\sin(b)$$

where $R_\odot = 8$ kpc is the adopted distance to the Galactic center, D is distance, and (l,b) are galactic coordinates. Note that the $Z = 0$ plane passes through the Sun, not the Galactic center (see J08), X axis points towards $l = 180°$ and Y axis points towards $l = 270°$ (disk rotation is towards $l \sim 90°$). We also use a cylindrical coordinate system defined by

$$R = \sqrt{X^2 + Y^2}$$
$$\phi = tan^{-1}\left(\frac{Y}{X}\right) \qquad (4)$$
$$\qquad (5)$$

Tangential velocity, v, is obtained from proper motion, μ, and distance D as:

$$v = 4.74\,\frac{\mu}{\mathrm{mas/yr}}\,\frac{D}{\mathrm{kpc}}\,\mathrm{km\,s^{-1}} \qquad (6)$$

Given radial (along the line of sight) velocity, v_{rad}, and two components of tangential velocity aligned with galactic coordinate system, v_l and v_b, the observed heliocentric Cartesian velocity components are computed from

$$v_X^{obs} = -v_{rad}\cos(l)\cos(b) + v_b\cos(l)\sin(b) + v_l\sin(l)$$
$$v_Y^{obs} = -v_{rad}\sin(l)\cos(b) + v_b\sin(l)\sin(b) - v_l\cos(l) \qquad (7)$$
$$v_Z^{obs} = -v_{rad}\sin(b) + v_b\cos(b)$$

These components are related to more traditional nomenclature as $v_X = -U$, $v_Y = -V$, and $v_Z = W$.

In order to obtain galactocentric cylindrical velocity components, v_R, v_ϕ and v_Z, corrections for solar motion must be applied. For the motion of the local standard of rest, we adopt $v_{LSR} = 220$ km s^{-1} (based on HI measurements by Gunn, Knapp & Tremaine 1979). For solar peculiar motion, we adopt HIPPARCOS-based results by Dehnen & Binney (1998): $v_X^{\odot,pec} = -10.0 \pm 0.4$ km s^{-1}, $v_Y^{\odot,pec} = -5.3 \pm 0.6$ km s^{-1}, and $v_Z^{\odot,pec} = 7.2 \pm 0.4$ km s^{-1}. Given the measured velocity components (eq. 7), the galactocentric components are obtained by adding solar motion

$$v_i = v_i^{obs} + v_i^\odot, \quad i = X, Y, Z, \qquad (8)$$

with $v_X^\odot = -10$ km s^{-1}, $v_Y^\odot = -225$ km s^{-1}, and $v_Z^\odot = 7$ km s^{-1} (note that $v_Y^\odot = -v_{LSR} + v_Y^{\odot,pec}$).

Finally, the cylindrical components, v_R and v_ϕ, can be computed using a simple coordinate system rotation

$$v_R = v_X\frac{X}{R} + v_Y\frac{Y}{R}$$
$$v_\phi = -v_X\frac{Y}{R} + v_Y\frac{X}{R} \qquad (9)$$

We discuss attempts to directly determine solar peculiar motion and v_{LSR} from our data in next two sections.

2.9. *A summary of the first two papers*

For completeness, we summarize the main results from J08 and I08 relevant for this work.

Using photometric data for 50 million stars from SDSS Data Release 4, sampled over distance range from 100 pc to 15 kpc, J08 showed that the stellar number density distribution, $\rho(R, Z, \phi)$ can be well described (apart from local overdensities; the J08 best-fit was refined using residual minimization algorithms) as a sum of two cylindrically symmetric components

$$\rho(R, Z, \phi) = \rho_D(R, Z) + \rho_H(R, Z). \tag{10}$$

The disk component can be modeled as a sum of two exponential disks

$$\rho_D(R, Z) = \rho_D(R_\odot) \times$$
$$\left[e^{-|Z+Z_\odot|/H_1 - (R-R_\odot)/L_1} + \epsilon_D e^{-|Z+Z_\odot|/H_2 - (R-R_\odot)/L_2} \right], \tag{11}$$

and the halo component requires an oblate power-law model

$$\rho_H(R, Z) = \rho_D(R_\odot) \epsilon_H \left(\frac{R_\odot^2}{R^2 + (Z/q_H)^2} \right)^{n_H/2}. \tag{12}$$

The best-fit parameters are discussed in detail by J08. We have adopted the following values for parameters relevant in this work (second column in Table 10 from J08): $Z_\odot = 25$ pc, $H_1 = 245$ pc, $H_2 = 743$ pc, $\epsilon_D = 0.13$, $\epsilon_H = 0.0051$, $q_H = 0.64$, and $n_H = 2.77$. The normalization $\rho_D(R_\odot)$ (essentially the local luminosity function for main sequence stars) is listed in J08 as a function of color.

Using photometric metallicity estimator for F/G main-sequence stars, I08 obtain an unbiased, three-dimensional, volume-complete metallicity distribution of ∼2.5 million F/G stars at heliocentric distances of up to ∼8 kpc. They found that the metallicity distribution functions (MDF) of the halo and disk stars are clearly distinct. The median metallicity of the disk exhibits a clear vertical (with respect to the Galactic plane; Z) gradient, and no gradient in the radial direction (for $Z > 0.5$ kpc and $6 < R/\mathrm{kpc} < 10$).

Similarly to stellar number density distribution, $\rho(R, Z)$, the overall behavior of the MDF $p([Fe/H]|R, Z)$ can be well described as a sum of two components

$$p(x = [Fe/H]|R, Z, \phi) = [1 - f_H(R, Z)]\, p_D(x|Z) + f_H(R, Z)\, p_H(x), \tag{13}$$

where the halo-to-disk counts ratio is simply $f_H(R, Z) = \rho_H(R, Z)/[\rho_D(R, Z) + \rho_H(R, Z)]$.

The halo metallicity distribution, $p_H([Fe/H])$, is spatially invariant and well described by a Gaussian distribution centered on $[Fe/H] = -1.46$, and with the intrinsic (not including measurement errors) width $\sigma_H = 0.30$ dex. For $|Z| \lesssim 10$ kpc, an upper limit on the halo radial metallicity gradient is 0.005 dex/kpc.

The disk metallicity distribution varies with Z such that its shape remains fixed, while its median, μ_D, varies as

$$\mu_D(Z) = \mu_\infty + \Delta_\mu \exp(-|Z|/H_\mu) \text{ dex}, \tag{14}$$

with the best-fit parameter values $H_\mu = 0.5$ kpc, $\mu_\infty = -0.82$ and $\Delta_\mu = 0.55$). The *shape* of the disk metallicity distribution can be modeled as

$$p_D(x = [Fe/H]|Z) = 0.63\, G[x|\mu = a(Z), \sigma = 0.2] +$$
$$0.37\, G[x|\mu = a(Z) + 0.14, \sigma = 0.2], \tag{15}$$

where the position a and the median μ_D are related via $a(Z) = \mu_D(Z) - 0.067$ (unless measurement errors are very large).

In this paper, we extend these models to kinematics.

3. ANALYSIS OF PROPER MOTION SAMPLE

We begin by analyzing proper motion measurements for stars observed towards the North Galactic pole. Towards this region, the rotational (azimuthal) velocity component, v_ϕ, and the radial velocity component, v_R, can be determined with sufficient accuracy from the proper motion measurements alone (i.e. without knowing the radial velocity, v_{rad}). This analysis yields significant insight in the kinematic behavior as a function of metallicity and distance from the galactic plane, Z. We then extend our analysis to the whole meridional $Y = 0$ plane and study the variation of kinematics as a function of both R and Z. We only consider the northern Galactic hemisphere, where most of the proper motion data are available.

3.1. *Kinematics towards the North Galactic pole*

We select subsamples of 14,000 disk stars and 23,000 halo stars towards the North Galactic pole by requiring $b > 80$ and $Z < 7$ kpc, and a sample of 105,000 red stars with $Z < 1$ kpc. The large number of stars allows us to directly map the v_ϕ vs. v_R velocity distribution function, even when simultaneously using narrow bins of metallicity and Z coordinate.

An example for ∼6,000 blue stars from the $Z = 4 - 5$ kpc range is shown in Figure A2. In this figure, and all other figures showing two-dimensional projections of velocity distribution, we use two visualization methods. The color-coded maps show smoothed counts, using a Bayesian density estimator developed by Ivezić et al. (2005, see their Appendix for derivation and discussion). At an arbitrary position, the density implied by sparsely sampled points is evaluated as

$$\rho = \frac{C}{\sum_{i=1}^{N} d_i^2}, \tag{16}$$

where d_i is the distance to the i-th neighbor (in the velocity-velocity plane), and N is the number of neighbors (we use $N = 10$). The simplest way to evaluate normalization constant C is to require that density ρ summed over all pixels is equal to the number of data points. The grid size is arbitrary, but the map resolution is of course controlled by the number of points. We choose pixel size roughly equal to one half of the measurement errors. As shown by Ivezić et al., this method is superior to simple Gaussian smoothing. For comparison, we also visualize the distributions using linearly-spaced contours.

Figure A2 demonstrates that kinematics strongly vary with metallicity, from non-rotating low-metallicity subsample with large velocity dispersion to rotating high-metallicity sample with much smaller dispersion. There is substantial substructure in the distributions, which is even more discernible for red stars, shown in Figure A3. The variation of kinematics with distance from the plane for red stars is remarkable. The substructure seen in the closest bin is very similar to the substructure seen in the local HIPPARCOS sample (Dehnen 1998). Note that, unlike Dehnen's result which was based on maximum likelihood analysis over the whole sky, our map is based on simple direct mapping of the velocity distribution of stars selected from a small sky region (∼300 deg^2). The similarity between the two velocity distributions, including multi-modal behavior reminiscent of Eggen's groups, is thus very striking, especially given the vastly different data sources.

COMMENT: Add a U-V plot with Eggen's groups on the same scale as Dehnen's plot.

We proceed by focusing analysis on blue stars, which sample the largest distance range. For a detailed study of the velocity distribution of nearby red stars, including a discussion of non-gaussianity, vertex deviation and difficulties with traditional thin/thick disk separation, we refer the reader to Kowalski et al. (in prep.).

The dependence of the median rotational velocity and its dispersion for both subsamples is shown in Figure A4. The two subsamples display remarkably different kinematic behavior. While this conclusion is qualitatively the same as discussed in the seminal paper by Eggen, Lynden-Bell & Sandage (1962), the new data analyzed here allow us to extend their result beyond the solar neighborhood to a ~ 100 times larger distance limit, and reproduce it *in situ* with a ~ 100 times larger sample.

Halo stars show small prograde rotation, at the level of about 20 km/s. Given systematic errors in proper motion and distance, this value is consistent with no motion. We have performed the same analysis on a sample with proper motions based only on POSS data, with SDSS positions not used in the proper motion fit (not publicly available). While random proper motion errors become larger, the median velocity decreases to only 5 km/s. This test suggests that the leading contribution to systematic proper motion errors could be a difference between SDSS (digital data) and POSS (digitized photographic data) centroiding algorithms. In addition, Smith et al. (2009) did not detect halo rotation using proper motion measurements that are based only on SDSS data (and thus probably have much smaller systematic errors than SDSS-POSS proper motion measurement analyzed here). We conclude that at the 10 km s^{-1} uncertainty level, there is no evidence for halo rotation towards the north galactic pole.

The measured dispersion increases with Z, but when random measurement errors (due to intrinsic scatter in photometric parallax relation, metallicity errors and proper motion errors) are taken into account, the data are consistent with a constant dispersion of $\sigma_\phi^H = 85$ km/s, with an uncertainty of about 5 km/s.

Disk stars display a decrease of rotational velocity with Z (sometimes called velocity lag, or velocity shear; see Section 3.4 in I08 for more details). In agreement with a preliminary analysis presented in I08, we find that the observed behavior in the $Z = 1 - 4$ kpc range can be described by

$$\langle v_\phi \rangle = -205 + 19.2 \, |Z/\mathrm{kpc}|^{1.25} \text{ km/s.} \tag{17}$$

The measured dispersion for disk stars increases with Z faster than can be attributed to measurement errors. Using a functional form $\sigma = a + b|Z|^c$, we find that the following *intrinsic* velocity dispersion is required by the data

$$\sigma_\phi^D = 30 + 3 \, |Z/\mathrm{kpc}|^{2.0} \text{ km/s.} \tag{18}$$

This function is shown by the dotted line in the bottom right panel in Figure A4. I08 forced a linear dependence on Z, but the difference between this result and their eq. 15 never exceeds 5 km/s for $Z < 3$ kpc. The errors for the power-law exponents for both eq. 17 and eq. 18 are ~ 0.1.

However, the simplistic description of the velocity distribution based on its first and second moments (eqs. 17 and 18) does not fully capture detailed data behavior. As already discussed by I08, the rotational velocity distribution for disk stars is strongly non-gaussian (see their Fig.13). It can be formally described by a sum of two gaussians with a fixed normalization ratio and a fixed offset of their mean values

$$p_D(x = v_\phi|Z) = 0.75 \, G[x|v_n(Z), \sigma_1] +$$
$$0.25 \, G[x|v_n(Z) - 34 \, \mathrm{km/s}, \sigma_2], \tag{19}$$

where

$$v_n(Z) = -194 + 19.2 \, |Z/\mathrm{kpc}|^{1.25} \text{ km/s.} \tag{20}$$

The intrinsic velocity dispersions σ_1 and σ_2 are modeled as $a + b|Z|^c$, with the best-fit parameters listed in Table 1 (see σ_ϕ^1 and σ_ϕ^2). Closer to the plane, in the $0.1 < Z < 2$ kpc range probed by red stars, the median rotational velocity and velocity dispersion are consistent with extrapolation of fits derived here using much more luminous blue stars.

Figure A5 shows v_ϕ distribution for several bins of distance from the plane, Z (analogous to Fig.13 from I08, except for showing v_ϕ instead of v_Y). In the best fits shown in figure, the values of measurement errors and $v_n(Z)$ are allowed to float. Yet, they never drift by more than 10 km/s from expected values; while such deviations could be evidence of kinematic substructure, they are also consistent with plausible systematic errors. We conclude that eqs. 19 and 20 provide a good description of disk kinematics for stars observed towards the north galactic pole.

The dependence of the median radial velocity (v_R, not the spectroscopic radial velocity along the line of sight, v_{rad}) and its dispersion for halo and disk subsamples is shown in Figure A6. The median values are consistent with zero within the plausible systematic errors (10-20 km/s) at all Z. Intrinsic dispersion for halo stars is consistent with a constant value of $\sigma_R^H = 135$ km/s, with an uncertainty of about 5 km/s. For disk stars, the best-fit functional form $\sigma = a + b|Z|^c$ is

$$\sigma_R^D = 40 + 5 \, |Z/\mathrm{kpc}|^{1.5} \text{ km/s.} \tag{21}$$

The σ_R^D/σ_ϕ^D ratio has a constant value of ~ 1.35 for $Z < 1.5$ kpc, and decreases steadily at larger Z to 1 at $Z \sim 4$ kpc.

3.2. *Kinematics in the Meridional $Y \sim 0$ Plane*

The analysis of rotational velocity component can be extended to the whole meridional plane defined by $Y = 0$. Close to this plane ($l \sim 0$ and $l \sim 180°$), the longitudinal proper motion approximately depends only on the rotational velocity component while latitudinal proper motion is a linear combination of radial and vertical components

$$v_b = \sin(b)v_R + \cos(b)v_Z. \tag{22}$$

Figure A7 shows the median v_ϕ and v_b as functions of R and Z, for halo and disk subsamples. The median v_b is everywhere close to zero as would be expected if the median v_R and v_Z are zero (the behavior of v_Z is discussed in the next section). One exception is a narrow feature with $v_b \sim -100$ km s^{-1} for $R < 4$ kpc. While a cold stellar stream would produce such a signature, it is surprising that its narrow geometry points directly at the observer. This is consistent with a localized systematic proper motion error and, indeed, the bottom left panel in Figure A1 shows that systematic latitudinal proper motion error towards $l \sim 0$ and with $b \sim 45°$ is about 1 mas/yr. This proper motion error corresponds to a velocity error of ~ 100 km s^{-1} at a distance of 7 kpc.

For halo stars, the median v_ϕ is close to zero for $R < 12$ kpc. In the region with $R > 12$ kpc and $Z < 6$ kpc, the median indicates surprising prograde rotation in excess of 100 km/s. However, Monoceros stream is found in this region. Since its metallicity is right at the adopted disk/halo separation boundary, and

because it rotates even faster than disk stars (see I08), it is likely that it is responsible for the observed behavior. Similar effect is seen for disk stars. There is also an indication of localized retrograde rotation for halo stars with $R \sim 15$ kpc and $Z = 8-9$ kpc. The same region also shows anomalous dispersion in the line-of-sight velocity, so most likely it is not a proper motion problem.

In order to visualize the extent of "contamination" by Monoceros stream, we replace the rotational velocity for each disk star by a simulated value drawn from distribution described by eq. 19. The model-based map and (data-model) residual map are shown in Figure A8. As evident, the position of the largest deviation is in excellent agreement with the position of Monoceros stream quantified in I08.

In order to further test the assertion that Monoceros stream biases otherwise simple gross kinematic behavior of disk and halo stars, we analyze v_ϕ vs. $[Fe/H]$ distributions for blue stars in the $Z = 4-6$ kpc range, as a function of R (see Figure A9). As evident in the bottom right panel, there is a significant excess of stars with $-1.5 < [Fe/H] < -0.5$ which rotate with ~ 200 km/s at $R > 17$ kpc, supporting the above conclusion.

The proper motion analysis presented in this section did not provide any constraints for the behavior of vertical velocity component, v_Z. The analysis of v_Z behavior requires line-of-sight radial velocity measurements, described next.

COMMENT: make also v_ϕ vs. $[Fe/H]$ plot for R=15–17 and Z=8–10.

4. ANALYSIS OF SPECTROSCOPIC SAMPLE

The SDSS spectroscopic sample of $\sim$100,000 main-sequence stars is much smaller than the proper motion sample and thus it has relatively poor spatial resolution for mapping variation of kinematics with position. Nevertheless, it is very valuable because it enables a direct[24] study of the distribution of all three velocity components to a distance of $\lesssim 10$ kpc, and can deliver velocity errors as small ~ 10 km s^{-1} at such distances (for blue stars; corresponding tangential velocity errors are about ~ 150 km s^{-1} at a distance of 10 kpc).

For each object in the SDSS spectroscopic survey, its spectral type, redshift (i.e., radial velocity in case of stars), and redshift error are determined by matching the measured spectrum to a set of templates. The stellar templates are calibrated using the ELODIE stellar library. Random errors for the radial velocity measurements are a strong function of spectral type and signal-to-noise ratio, but are usually < 5 km s^{-1} for stars brighter than $g \sim 18$, rising sharply to ~ 15 km s^{-1} for stars with $r = 20$. We model this behavior of radial velocity errors as

$$\sigma_{rad} = 3 + 12 \, 10^{0.4(r-20)} \, \text{mas/yr}. \tag{23}$$

We begin our analysis using distant blue disk and halo stars, and then briefly discuss kinematics of less distant M stars.

4.1. *Blue main-sequence stars*

In order to maximize the sample distance limit, we select 42,000 stars with $0.2 < g-r < 0.6$ (29,000 have $b > 0$). Using spectroscopic metallicity, we separate them into 28,500 candidate halo stars with $-3 < [Fe/H] < -1.1$, and $\sim 10,000$ disk stars with $-0.9 < [Fe/H] < 1$. We estimate that the application of photometric metallicity for disk/halo classification would result in a contamination rate of 14% for both subsamples.

The dependence of the median vertical velocity (v_Z) and its dispersion for halo and disk subsamples is illustrated in Figure A10. The median values of v_Z are consistent with zero to better than 10 km s^{-1} at $Z < 5$ kpc, where statistical fluctuations are small. We have corrected radial velocity measurements for a systematic error of 6 km s^{-1}, discussed further below.

Similarly to the other two velocity components, data can be modeled using a constant dispersion for halo stars ($\sigma_Z^H = 85$ km s^{-1}), while for disk stars, the best-fit functional form $\sigma = a + b|Z|^c$ is

$$\sigma_Z^D = 25 + 4 |Z/\text{kpc}|^{1.5} \, \text{km s}^{-1}. \tag{24}$$

The σ_R^D / σ_Z^D ratio decreases steadily from ~ 1.6 for $Z \sim 1$ kpc to 1.4 at $Z \sim 4$ kpc. Other two velocity components for spectroscopic sample display the same behavior as the proper motion sample shown in Figures A4 and A6, except for slightly different error properties. This is encouraging because spectroscopic sample is collected over the whole northern hemisphere, unlike the proper motion sample which is limited to $b > 80°$.

The availability of all three velocity components for spectroscopic sample makes it possible to study the orientation of velocity ellipsoid. Figure A11 shows three two-dimensional projections of the velocity distribution for two subsamples of candidate halo stars with $0.2 < g-r < 0.4$ selected from two narrow ranges of distance from the plane ($|Z| = 3-4$ kpc, above and below the plane). A striking feature in this figure is strong evidence for velocity ellipsoid tilt in top and bottom left panels. Not only that kinematics "know" whether stars come from northern or southern hemisphere, but the direction of velocity ellipsoid "knows" where the Galactic center is! While the tilt angle errors are too large to obtain a significant improvement in the measurement of $R_\odot$ (a plausible, if somewhat optimistic, tilt angle uncertainty of 1° corresponds to $R_\odot$ error of 0.5 kpc; extending the sample to $|Z| = 8$ kpc could deliver errors of 0.3 kpc per bin of a similar size), it is remarkable that the northern and southern subsamples agree so well. In addition, when the northern sample (with $|Z| = 3-4$ kpc) is divided into two subsamples with $R = 5-7$ kpc and $R = 10-13$ kpc, the tilt angle varies by the expected $\sim 6°$ in correct direction. Even for a very small sample of 270 stars with $|Z| = 5-7$ kpc and $R = 6.5-7.5$ kpc, the best fit tilt angle is statistically consistent (within 5°) with the expected value of 36°.

Other two projections of velocity distribution for halo stars do not show significant tilt. Using velocities transformed to spherical coordinate system,

$$v_r = v_R \frac{R}{R_{gc}} + v_Z \frac{Z}{R_{gc}}$$
$$v_\theta = v_R \frac{Z}{R_{gc}} - v_Z \frac{R}{R_{gc}}, \tag{25}$$

where $r = R_{gc} = (R^2 + Z^2)^{1/2}$ is spherical galactocentric radius, we find no statistically significant tilt of v_r vs. v_θ, nor any other two-dimensional projection (with tilt angle errors ranging from about 1° to about 5°, depending on sample size and median R and Z).

The strong evidence for the tilt of the v_Z vs. v_R velocity ellipsoid seen for low-metallicity candidate halo stars is not seen for disk stars. Figure A12 shows two-dimensional projections of the velocity distribution for two subsamples of candidate disk stars with $0.2 < g-r < 0.4$ selected from two narrow ranges

---

[24]Statistical deprojection methods, such as that recently applied to a subsample of M stars discussed here by Fuchs et al. (2009) can be used to indirectly infer the three-dimensional kinematics.

of distance from the plane ($|Z| = 1.5 - 2.5$ kpc, above and below the plane). The smaller Z range is mandated by sample contamination: larger $|Z|$, which would provide more signal for velocity ellipsoid tilt (at a constant R), have fewer stars and suffer from increased contamination by halo stars. Within $\sim 1\sigma$, the velocity tilt is consistent with zero. The alignment of the velocity ellipsoid with spherical coordinate system is ruled out at about 2σ or greater significance level for each of 5 analyzed $R-Z$ bins with $|Z| = 1.5 - 2.5$ kpc and $R = 6 - 11$ kpc, with R bin size of 1 kpc. We conclude that there is no statistical evidence for the velocity ellipsoid tilt for disk stars, but caution that, due to small Z range, the data cannot easily distinguish cylindrical and spherical alignment.

The v_ϕ vs. v_R velocity distributions for both the northern and southern subsamples (top and bottom middle panels in Figure A12) suggest a misalignment with the coordinate axes, usually interpreted as vertex deviation (analogous to velocity ellipsoid tilt discussed above, but defined in the v_ϕ vs. v_R plane instead of the v_Z vs. v_R plane). Another interpretation invokes a multi-component velocity distribution, which can result in a similar deviation even if each component is perfectly symmetric in cylindrical coordinate system. Because the spectroscopic samples are not large enough, these two possibilities are hard to distinguish observationally (but see below).

4.2. *Red main-sequence stars*

The complex v_ϕ vs. v_R distribution for blue disk stars seen in Figure A12 ($Z \sim 2$ kpc) can be traced closer to plane ($Z < 2$ kpc) with red spectroscopic stars. The middle top and left panels in Figure A13 show the v_ϕ vs. v_R distribution for red ($g-r > 0.6$, median 1.2) stars with $|Z| = 0.6 - 0.8$ kpc. In both hemispheres, data are consistent with a vertex deviation of about $20°$, similar to values obtained by Fuchs et al. (2009).

However, Kowalski et al. (in prep.) demonstrate that ambiguous interpretation of spectroscopic samples can be disambiguated by proper motion samples of red stars observed towards the north galactic pole. The v_ϕ vs. v_R distribution for red stars in their sample, with $0.1 < Z/\text{kpc} < 1.5$, can be fit by a sum of two gaussian distributions that are offset from each other by ~ 10 km s^{-1} in each direction. This offset results in a non-zero vertex deviation if the sample is not large enough, or measurements are not accurate enough, to resolve two gaussian components. This double-gaussian structure is clearly at odds with classical description based on the Schwarzschild approximation. We refer the interested reader to the Kowalski et al. study for more details.

4.3. *Direct determination of solar peculiar motion*

Assuming there is no net streaming motion in the Z direction in the solar neighborhood, the median heliocentric v_Z^{obs} for stars both above the plane ($Z > 0$) and below the plane should be equal to $v_Z^\odot$ (7 km s^{-1} based on analysis of HIPPARCOS results by Dehnen & Binney, 1998). Even if there is bulk streaming motion, the median heliocentric v_Z^{obs} should still be the same for subsamples selected above and below the plane (unless the bulk flow would suddenly change its velocity in the solar neigborood). We find that this is not the case for the data used here.

In order to limit the averaging volume to about 1 kpc (so that the assumption of constant bulk streaming motion is likely correct), we select $\sim 13{,}000$ stars with $2.3 < g-i < 2.8$ from the spectroscopic sample. Stars from the northern hemisphere (5,700) have a median heliocentric $\langle v_Z^{obs} \rangle = -1.8$ km s^{-1}, while for stars from the southern hemisphere $\langle v_Z^{obs} \rangle = -11.0$ km s^{-1}. This difference can be interpreted as due to a systematic radial velocity error. By simultaneously varying an assumed error, Δ_{rad}, and $v_Z^\odot$, with a requirement that the median v_Z^{obs} should be the same for both hemispheres, we obtain $\Delta_{rad} = 5.0$ km s^{-1} and $v_Z^\odot = 6.5$, with uncertainties of 0.4 km s^{-1}. This value for $v_Z^\odot$ is in excellent agreement with HIPPARCOS-based value of 7.2 ± 0.4 km s^{-1} (Dehnen & Binney 1998). COMMENT: anything intelligent to add about ELODIE spectra? Is $\Delta_{rad} = 5.0$ km s^{-1} plausible?

When $\Delta_{rad} = 5.0$ km s^{-1} is subtracted from all SDSS radial velocity measurements, the median v_Z for all color-selected subsamples are consistent with zero everywhere except for blue low-metallicity stars with $Z < 2$ kpc from the southern galactic hemisphere ($l = 40° - 150°$ and $|b| = 25° - 65°$): for these stars the median v_Z is about 15 km s^{-1}. This median does not vary with b, suggesting that this offset is probably not due to systematic errors in proper motion or radial velocity measurement. In addition, a subsample with $[Fe/H] > -1$, which otherwise has similar apparent magnitude and sky distributions, does not show this offset.

If the adopted value of $v_X^\odot = -10$ km/s were incorrect, the median v_R would deviate from zero. The variance of median v_R for samples of nearby M stars selected by distance and color is 0.5 km s^{-1}, which is an upper limit for the error in adopted value $v_X^\odot$. This result, based on full three-dimensional velocities agrees with results from indirect methods based only on proper motions for nearby HIPPARCOS sample (Dehnen 1998), and for SDSS M dwarf sample (Fuchs et al. 2009).

For both blue and red disk stars, the extrapolation of median v_ϕ to $Z = 0$ gives -205 km s^{-1}. Since the correction of observed velocities assumed a solar motion of -225 km s^{-1}, this extrapolation implies that the Y component of the Sun's velocity relative to the bulk motion of the solar neighborhood is 20 km s^{-1}, again in agreement with the recent results by Fuchs et al. (but note that both results are based on the same data COMMENT: Fuchs et al. used mean, and here we use median; how can they be the same given skewed distribution??). Dehnen & Binney (1998) obtained a similar value[25] for their subsample of red stars within 100 pc.

5. A MODEL FOR KINEMATICS OF DISK AND HALO STARS

Informed by the results from preceding two sections, here we introduce a model that aims to describe the global behavior of stellar kinematics. This model is certainly wrong and insufficient. It is wrong because we don't attempt to account for kinematic substructure (e.g. Monoceros stream, which rotates faster than disk stars in which it is embedded, and also has a distinctive metallicity distribution, see I08), and it is insufficient because it does not address the bulge region, nor does it account for complex kinematic behavior close to the galactic plane. Nevertheless, this model captures the gross data behavior in the volume probed by SDSS, including the significant kinematic difference between high-metallicity disk stars and low-metallicity halo stars. We first describe the model, and then test it using both proper motion and radial velocity samples.

5.1. *Halo Kinematics*

---

[25]Dehnen & Binney extrapolated the mean azimuthal motion of color-selected samples, which is correlated with the radial velocity dispersion, to zero dispersion and obtained $v_Y^{\odot,pec} = -5.3$ km s^{-1}, used here.

Similarly to its metallicity distribution, the kinematics of halo stars are by and large spatially invariant. The only significant spatial variation is that of the velocity ellipsoid tilt angle. However, when cylindrical velocity components are expressed in spherical coordinate system, a single velocity ellipsoid becomes a good description of halo kinematics throughout the probed volume (apart from localized substructures such as Monoceros stream).

Our model assumes that halo does not have net rotation (see below for a test of this assumption), and that principal axes are aligned with spherical coordinate system. The velocity dispersions measured in preceding two sections (in Section 3, we determined $\sigma_R^H = 135$ and $\sigma_\phi^H = 85$, and $\sigma_Z^H = 85$ in Section 4) are expressed in cylindrical coordinate system. We have used Monte Carlo simulations to translate them to spherical coordinate system (the interplay between proper motion, radial velocity and distance measurement errors is exceedingly complex). We obtained $\sigma_r^H = 141$ and $\sigma_\theta^H = 75$, with probable uncertainties of about 5 km s^{-1}.

5.2. *Disk Kinematics*

Closer than about 1-2 kpc from the galactic plane, the measurement errors are sufficiently small and samples are sufficiently large to resolve rich kinematic substructure (e.g., see Figure A3). This behavior is quantified in detail in Kowalski et al. Here we simply use eqs. 19 and 20) to describe non-gaussian v_ϕ distribution and velocity shear for disk stars, and assume that v_R and v_Z distributions are un-correlated gaussian distributions with zero means and Z-dependent intrinsic dispersions listed in Table 1.

As discussed in section 4, there is no strong evidence that blue disk stars display a tilt of velocity ellipsoid in the $v_R - v_Z$ plane. A vertex deviation is clearly seen in the data for $Z < 1$ kpc, but as shown by Kowalski et al., it appears to be a consequence of two-component nature of the underlying $v_R - v_\phi$ velocity distribution.

5.3. *Global Model Tests*

Our model predicts distributions of the three measured kinematic quantities, v_{rad}, μ_l and μ_b. A simple model test is to compute the mean and the distribution width for (data-model) residuals normalized by predicted dispersions

$$\chi = \frac{d - m}{(\sigma_d^2 + \sigma_m^2)^{1/2}}, \qquad (26)$$

where σ_d is measurement error and σ_m is the dispersion predicted by the model. We find that the mean value of χ is 0 to within 0.05 for all three quantities, with dispersions about 1.05-1.1. While this result is a necessary condition for model to be accepted, it is not sufficient. There may be various trends in residuals that are not easily uncovered by the overall χ statistic, and thus we perform further tests for various judiciously selected subsamples.

Figure A5 represents a strong test of the model proposed here, including both disk kinematics, with its shear and non-gaussian v_ϕ profile, and halo kinematics. However, this test is valid only for a small region around the north galactic pole. Its extension to the whole meridional plane is shown in Figure A8 for disk stars. Here we perform additional tests that cover the entire sky region with available data.

Figure A14 compares medians and dispersions for measured and modeled radial velocity of halo stars. The elongated velocity ellipsoid aligned with spherical radius is nicely seen in the

dispersion gradient from the inner to outer Galaxy (bottom left panel). There are no large discrepancies between measured and predicted behavior. Pixel-to-pixel scatter of the difference of medians is 21 km s^{-1}, which is about the same as the scatter between two model realizations. The data/model dispersion ratio is centered on 1.13, with a scatter of 0.2. For pairs of model realizations, the ratio is always centered on 1 to within 0.02, with a scatter of 0.2. Hence, we are finding that the observed velocity dispersion is about 10% larger ($\sim$10 km s^{-1}) than predicted by our smooth model. Results for disk stars are similar.

Proper motion sample has many more stars, which enables a much higher spatial resolution when searching for structure in model residuals (on the other hand, radial velocity measurement errors do not increase with distance as fast as tangential velocity errors, which makes radial velocity superior at large distances). We have compared observed and modeled proper motion distributions in narrow bins of distance, across the sky, and separately for disk and halo subsamples. As an illustration, Figures A15 and A16 show the median longitudinal and latitudinal proper motion observed for disk stars. There is very little change in the proper motion distribution among different distance bins because of vertical rotational velocity gradient which is nearly linear. Model distributions look identical to the eye. The (data-model) residuals for longitudinal proper motion are shown in Figure A17. They provide weak evidence for a radial gradient that is not modeled, or for substructure, but it is not easy to distinguish these two possibilities.

A comparison of disk and halo subsamples selected from the same distance bin ($\sim$4 kpc) is shown in Figure A18. The largest data vs. model discrepancy for halo stars, seen in the bottom left panel, is also seen from a different viewing angle in the top left panel in Figure A7.

We conclude that our model reproduces reasonably well the first and second moments of the velocity distributions for disk and halo stars, and the non-gaussian v_ϕ distribution for disk stars, except in the region close to Monoceros stream.

5.4. *Constraints of v_{LSR} from large-scale halo kinematics*

The halo proper motion distribution towards north galactic pole depends only on the difference between v_ϕ for the Sun and halo stars. However, for a sample extended over a large sky area, these two velocities are not degenerate any more and have different impacts on the predicted proper motion distributions. This can be used to obtain (weak, $\sim$20 km s^{-1}) constraints on both (the best fits are consistent with assumed values, $v_{LSR} = 20$ km s^{-1} and no halo rotation).

5.5. *Kinematic Parallax Relation*

Model constraints from proper motions involve a degenerate ratio of velocity and distance. Since velocity scale is set by radial velocity data, and the model agrees with the data, one can get constraints on distance errors by fitting proper motion distribution: kinematic parallax relation.

The errors in adopted photometric parallax relation are small, but need to redo analysis with DR7 proper motions.

6. SUMMARY AND DISCUSSION

This is the first analysis based on SDSS data that simultaneously studies kinematics of halo and disk populations, including halo samples studied by Carollo et al. (2007) and Smith et al. (2009), and disk samples ranging from nearby M stars (such as samples studied by Bochanski et al. 2007 and Fuchs et al. 2009) to distant F/G stars. We have quantified probability

distribution function $p_3(\mu_l, \mu_b, v_{rad}|u-g, g, g-r, l, b)$ introduced in I08 that describes proper motion and radial velocity measurements for a given bin in the g vs. $g-r$ color-magnitude diagram, as a function of position on the sky, and as a function of the $u-g$ color. We have developed a simple empirical model based on a sum of two components, for disk and halo, that map well to components detected in spatial profiles and metallicity distribution.

At nearest distances (< 100 pc) that were accessible to HIPPARCOS survey, we obtain encouraging agreement with results from Dehnen & Binney (1998) and Dehnen (1998). The extension of kinematic mapping to distances up to ~ 10 kpc represents significant observational breakthrough and delivers powerful new constraints for dynamical modeling of the Galaxy.

6.1. *Disk Kinematics*

The disk kinematics are dominated by a vertical (Z) gradient. The mean rotational velocity and the three velocity dispersions for disk stars can be modeled as relatively simple functions of the form $a + b|Z|^c$ (see eqs. 19 and 20, and Table 1). The shape of rotational velocity distribution for disk component is nongaussian and can be formally modeled as a sum of two gaussian components with fixed normalization ratio for $|Z| \gtrsim 1$ kpc.

The fact that the normalization ratio of these two components does not vary with Z is at odds with standard disk decomposition into thin and thick disk components (see also Sections and 3.4.4 and 4.2.1 in I08). Loebman et al. (2008) argued, based on the behavior of N-body models by Roškar et al. (2008), that the unexpected behavior of new data, including the absence of velocity-metallicity correlation at the thin/thick disk boundary pointed out by I08, may be due to a combination of strong vertical age gradient and radial migration of stars. A more detailed study will be presented by Loebman et al. (in prep.). A significant vertical age gradient for disk stars is also supported by analysis of active M dwarfs presented in Bochanski et al. (2007).

Close to the plane, proper motion data imply complex multimodal velocity distribution which is inconsistent with a description based on standard Schwarzschild ellipsoid. It is striking that we obtained essentially the same velocity distribution morphology by direct mapping as did Dehnen (1998) using a statistical deprojection method and HIPPARCOS data. Our results for the first and second moments of velocity distribution for nearby M stars agree with analogous results obtained recently by Fuchs et al. (2009). However, their interpretation should be cautious, especially for the orientation of the velocity ellipsoid, which is strongly affected by multi-modal structure. We discuss these issues in more detail in Kowalski et al. (in prep.).

6.2. *Halo Kinematics*

Our results for the velocity distribution of halo stars are in excellent agreement with Smith et al. (2009). Although their analysis was limited to about 30 times smaller sky area, they used proper motion measurements that are based only on SDSS data, and thus have significantly different, and most likely much smaller, systematic errors than SDSS-POSS proper motion measurements analyzed here (and somewhat larger random errors). Hence, the close agreement of our and their results for halo velocity ellipsoid orientation and size (we obtained $\sigma_r^H = 141$ km s^{-1}, $\sigma_\theta^H = 75$ km s^{-1}, and $\sigma_\phi^H = 85$ km s^{-1}, and their values are 142 km s^{-1}, 77 km s^{-1}, and 81 km s^{-1}, respectively) are encouraging. Their estimated errors of 2 km s^{-1} apparently do not include systematic effects (such as errors in photometric parallax; both studies used the same calibration from I08); based on our Monte Carlo simulations, we believe that true errors (including systematics) cannot be smaller than ~ 5 km s^{-1}. The measurement of the velocity ellipsoid for halo stars represents a strong constraint for the shape of gravitation potential, as discussed by Smith et al. (2009).

COMMENT: Notes: also mention Siebert et al. result for velocity ellipsoid tilt. Discuss Morrison et al. result for velocity dispersion in outer halo, and Carollo et al. results.

6.3. *Kinematic Substructure*

Data-model residuals can be used to search for low-level substructure with a high spatial resolution. Show examples.

Refer to recent studies based on angular momentum analysis, such as Klement et al. (2009)

6.4. *Future Work*

Tomography IV: Jurić et al. (in prep.) determine luminosity functions for disk and halo, and describe a publicly available tool for generating mock catalogs based on the models introduced in this series of papers.

Tomography V: Berry et al. (in prep.) descend into the disk by solving extinction problem (stars at small b are embedded in dust and thus SFD always gives overestimated extinction) via SED fitting of SDSS and 2MASS photometry. Yields both a three-dimensional extinction map for SEGUE data and distances to stars. The latter enable tomographic mapping all the way to $b = 0$. The best fits will be made publicly available.

6.5. *Future Surveys*

Pan-STARRS, SkyMapper, Dark Energy Survey, LSST: deeper, wider and better proper motions. Gaia: highly accurate trigonometric distances and proper motions to $r = 20$, radial velocities to $r = 16$. LSST will rule beyond 10 kpc.

APPENDIX

THE REVISED SDSS METALLICITY SCALE

Recent analysis of metallicity and kinematics for halo and disk stars by I08 utilized photometric metallicity estimates for F/G stars with $0.2 < g - r < 0.6$. Their mapping function from the $g - r$ vs. $u - g$ color-color diagram to metallicity was calibrated using stars with spectroscopic metallicities distributed in SDSS Data Release 6. At that time, high-metallicity stars required for the calibration of methods implemented in automated spectroscopic pipeline (SEGUE Stellar Parameters Pipeline; Beers et al. 2006) were not available. Between Data Releases 6 and 7, the required data were collected and the new calibration resulted in revised spectroscopic metallicity values distributed with Data Release 7 (Lee et al. 2007ab; Allende Prieto et al. 2007).

Here we recalibrate the photometric metallicity estimator using updated spectroscopic metallicities from Data Release 7. We also re-derive parts of I08 analysis that are most affected by this change of metallicity scale.

The updated photometric metallicity estimator

Figure A19 shows that the largest difference between SDSS spectroscopic metallicity values distributed with Data Releases 6 and 7 is at the high-metallicity end (as expected). In particular, the abrupt cut in the metallicity distribution at $[Fe/H] \sim -0.5$ (see Figure 9 in I08) is not present any more and the distribution extends to values as high as $[Fe/H] \sim -0.2$ (the distances for the shown stars range from ~ 1 kpc to ~ 7 kpc.

We proceed to re-derive the photometric metallicity calibration using the same selection criteria and the same methodology as in I08. The new data set admits a slightly simpler function. The complex dual definition of the x axis is not required any more and the new expression is

$$[Fe/H]_{ph} = A + Bx + Cy + Dxy + Ex^2 + Fy^2 + Gx^2y + Hxy^2 + Ix^3 + Jy^3, \tag{A1}$$

with $x = (u - g)$ and $y = (g - r)$. The best-fit coefficients are $(A-J) = (-13.13, 14.09, 28.04, -5.51, -5.90, -58.68, 9.14, -20.61, 0.0, 58.20)$. Note that the coefficient I is 0. We removed this term because with the new data set it was producing too much curvature at the right end (red $u - g$) of the best-fit map.

We estimate that an upper limit for the intrinsic metallicity scatter for fixed noiseless $u - g$ and $g - r$ colors (presumably due to limited sensitivity of broad-band colors to metallicity variations) is about 0.1 dex. This value is estimated from the scatter in the difference between spectroscopic and photometric metallicities, discussed below. Unlike I08, who simply adopted the median metallicity value given by the above expression for each star, we draw photometric metallicity estimates from a Gaussian distribution centered on the best-fit median value, and with a width of 0.1 dex. The main benefit is the avoidance of hard edges in the photometric metallicity distribution for stars close to the edges of the calibration region in the $g - r$ vs. $u - g$ diagram.

The performance of the new map is qualitatively the same as that of the old map. The median and scatter for the difference between spectroscopic and photometric metallicities as a function of the $g - r$ and $u - g$ colors are shown in the top two panels in Figure A20. Typical systematic errors in the map (i.e. median difference per pixel) are ~ 0.1 dex or smaller, and the scatter varies from ~ 0.2 dex at the high-metallicity end to ~ 0.3 dex at the low-metallicity end (note that this scatter includes contribution from errors in both spectroscopic and photometric metallicity).

The above photometric metallicity estimator is applicable for stars with $0.2 < g - r < 0.6$ and $-0.25 + 0.5 * (u - g) < g - r < 0.05 + 0.5(u - g)$ (i.e. for the calibration region in the $g - r$ vs. $u - g$ color-color diagram shown in the top two panels in Figure A20; these constraints isolate main sequence F and G stars). It should be noted that the performance of photometric metallicity estimator deteriorates at the low-metallicity end because the $u - g$ color becomes insensitive to further metallicity decrease. As shown in the bottom left panel in Figure A20, the photometric metallicity saturates at $[Fe/H] \sim -2$ for smaller values of spectroscopic metallicity. For example, for spectroscopic metallicity of $[Fe/H] = -2.5$, the photometric metallicity is overestimated by as much as 0.5 dex. This shortcoming could be alleviated by using more accurate u band photometry (say, with errors of 0.01 mag instead of 0.03 mag as used here), but probably not for metallicities lower than $[Fe/H] = -2.5$. Fortunately, the low-metallicity halo stars within SDSS reach have a median metallicity of $[Fe/H] \sim -1.5$ (I08). Another important note is that, despite the improvement at the high-metallicity end, the calibration range only extends to $[Fe/H] \sim -0.2$. Any result relying on higher metallicities should be interpreted with caution (especially at low galactic latitudes where the uncertain ISM extinction may strongly affect the estimated metallicities). For stars with spectroscopic metallicity $[Fe/H] > -2.2$, the distribution of the difference between spectroscopic and photometric metallicities is well described by a Gaussian with a width of 0.26 dex (see the bottom right panel in Figure A20).

Tomography II reloaded

I08 pointed out several aspects of their analysis that may have been affected by the DR6 metallicity "compression" at the high-metallicity end. We repeated their full analysis and report here on those aspects where differences warrant discussion.

The "hard" upper limit for photometric metallicity estimates at the high-metallicity end ($[Fe/H] \sim -0.5$) with DR6 calibration is best seen in the bottom left panel in Figure 9 from I08. We reproduce that map of the conditional metallicity distribution in the top

left panel in Figure A21. As expected, the metallicity distribution of disk stars within 2 kpc from the Galactic plane now extends to $[Fe/H] \sim 0$.

Due to the change in calibration, the parameters of the best-fit expression that describes the variation of the median metallicity for disk stars as a function of the distance from the Galactic plane

$$\mu_D(Z) = \mu_\infty + \Delta_\mu \exp(-|Z|/H_\mu) \text{ dex}, \tag{A2}$$

are also changed. The updated values are $H_\mu = 0.5$ kpc, $\mu_\infty = -0.82$ and $\Delta_\mu = 0.55$ (the old values were $H_\mu = 1.0$ kpc, $\mu_\infty = -0.78$ and $\Delta_\mu = 0.35$). The best-fit values of μ_∞ and Δ_μ are constrained to within ~ 0.05 dex. The values of H_μ in the range 350–700 pc are consistent with the data. Another reason for a decrease in H_μ is an additional requirement that the best-fit function must satisfy the local constraint $\mu_D(Z) = -0.2$ (Nordström et al. 2004; Allende Prieto et al. 2004).

An interesting result from I08 was statistical detection of disk stars at a distance from the Galactic plane as large as ~ 6 kpc (see their Figure 10). A peak at $[Fe/H] = -0.5$ in the metallicity distribution of stars at those distances was another manifestation of the metallicity "compression". As demonstrated in the top right panel in Figure A21, this peak is not present when using the revised calibration. However, there is still statistical evidence that disk stars exist at such large distances from the plane: about 5% of stars in the 5 kpc $< Z <$ 7 kpc bin are presumably disk stars, in agreement with extrapolation of the exponential profile for counts of disk stars.

Perhaps the most intriguing result of I08 study was the non-detection of a correlation between rotational velocity and metallicity for disk stars at $Z \sim 1$ kpc. At such distances from the Galactic plane, the counts of thin and thick disk stars inferred from the spatial density profiles are expected to be similar. Since traditionally the thick disk component is associated with a larger velocity lag and lower metallicities, a fairly strong and detectable correlation was expected (see I08 for details). The two bottom panels in Figure A21 demonstrate that such a correlation is still undetected, although the photometric metallicity range now extends to higher values (up to $[Fe/H] \sim -0.2$).

The higher metallicity values obtained with re-calibrated relation have quantitative effect on the best-fit metallicity distributions shown in Figure 7 from I08. Using the same methodology, we reproduce their Figure as Figure A22 here. I08 modeled the non-Gaussian disk metallicity distribution using a sum of two Gaussians with a fixed amplitude ratio (1.7:1), fixed difference of the mean values (0.14 dex), and fixed widths (0.21 dex and 0.11 dex), which "slides" as a function of Z according to eq. A2. We find that the only required significant change is to increase the width of the second Gaussian to 0.21 dex, which accounts for the extension of the metallicity distribution to higher values. Only minor changes are required for the best-fit halo metallicity distribution (see Table 3 in I08): the median halo metallicity is now -1.46 in the first three bins, and -1.56 in the most distant Z bin, and its width changed from 0.32 dex to 0.36 dex in the last bin. We note somewhat less scatter of the data points around the best-fit functions with the re-calibrated data set. To summarize, the revised best-fit parameters that describe halo and disk metallicity distributions are:

- The halo metallicity distribution is spatially invariant and well described by a Gaussian distribution centered on $[Fe/H] = -1.46$, and with the intrinsic (not including measurement errors) width $\sigma_H = 0.30$ dex. For $|Z| \lesssim 10$ kpc, an upper limit on the halo radial metallicity gradient is 0.005 dex/kpc.

- The disk metallicity distribution varies with Z such that its shape remains fixed, while its median, μ_D, varies as given by eq. A2 (with the best-fit parameter values $H_\mu = 0.5$ kpc, $\mu_\infty = -0.82$ and $\Delta_\mu = 0.55$). The shape of the disk metallicity distribution can be modeled as

$$p_D(x = [Fe/H]|Z) = 0.63\,G[x|\mu = a(Z), \sigma = 0.2] + 0.37\,G[x|\mu = a(Z) + 0.14, \sigma = 0.2], \tag{A3}$$

where the position a and the median μ_D are related via $a(Z) = \mu_D(Z) - 0.067$ (unless measurement errors are very large).

We point out that the asymmetry of metallicity distribution for disk stars is now less pronounced (as implied by the same widths of the two best-fit Gaussian components). Nevertheless, due to large sample size, the non-gaussianity is statistically detected beyond doubt. A remaining concern is the error distribution for photometric metallicity, which itself could account for such a deviation from gaussianity. However, to the extent possible using highly incomplete spectroscopic sample (c.f. the bottom right panel in Figure A20 and discussion in I08), we are unable to quantitatively explain the observed deviation from gaussianity as an artifact of photometric metallicity method.

<div align="center">REFERENCES</div>

Abadi, M.G., Navarro, J.F., Steinmetz, M. & Eke, V.R. 2003, ApJ, 597, 21

Abazajian, K., Adelman, J.K., Agüeros, M., et al. 2003, AJ, 126, 2081

Abazajian, K., Adelman, J.K., Agüeros, M., et al. 2004, AJ, 129, 1755

Abazajian, K., Adelman, J.K., Agüeros, M., et al. 2005, AJ, 128, 502

Adelman-McCarthy, J.K., Agüeros, M.A., Allam, S.S., et al. 2006, ApJS, 162, 38

Allende Prieto, C., Barklem, P.S., Lambert, D.L. & Cunha, K. 2004, A&A, 420, 183

Allende Prieto, C., Beers, T.C., Wilhelm, R. et al. 2006, ApJ. 636, 804

Allende Prieto, C., Sivarani, T., Beers, T.C., et al. 2007, submitted to AJ

Bahcall, J.N. & Soneira, R.M. 1980, ApJSS, 44, 73

Bailer-Jones, C.A.L., Irwin, M., Gilmore, G. & von Hippel, T. 1997, MNRAS, 292, 157

Bailer-Jones, C.A.L., Irwin, M. & von Hippel, T. 1998, MNRAS, 298, 361

Becker, A.C., Silvestri, N.M., Owen, R.E., Ivezić, Ž., & Lupton, R.H. 2007, PASP, 119, 1462

Beers, T.C., Drilling, J.S., Rossi, S., et al. 2002, AJ, 124, 931

Beers, T.C. & Christlieb, N. 2005, ARA&A, 43, 531

Beers, T.C., Lee, Y., Sivarani, T., et al. 2006, Mem.S.A.It., 77, 1171

Belokurov, V., Zucker, D.B., Evans, N.W., et al. 2006, ApJ, 642, L137

Belokurov, V., Evans, N.W., Irwin, M.J., et al. 2007, ApJ, 658, 337

Bensby, T., Feltzing, S. & Lundström, I. 2003, A&A, 410, 527

Bell, E.F., Zucker, D.B., Belokurov, V. et al. 2007, accepted to ApJ (also astro-ph/0706.0004)

Brook, C.B., Kawata, D., Gibson, B.K. & Freeman, K.C. 2004, ApJ, 612, 894

Bullock, J.S. & Johnston, K.V. 2005, ApJ, 635, 931

Carney, B.W. 1979, ApJ, 233, 211

Carollo, D., Beers, T.C., Lee, Y.S., et al. 2007, Nature, 450, 1020

Casagrande, L., Portinari, L. & Flynn, C. 2006, MNRAS, 373, 13
Chiba, M. & Beers, T.C. 2000, AJ, 119, 2843
Clem, J.L., VandenBerg, D.A. & Stetson, P. 2008,
Conn, B.C., Martin, N.F., Lewis, G.F., et al. 2005, MNRAS, 364, L13
Covey, K., Ivezić, Ž., Schlegel, D., et al. 2007, AJ, 134, 2398
Dehnen, W. & Binney, J.J. 1998, MNRAS, 298, 387
Demarque, P. & McClure, R.D. 1980, ApJ, 242, 5
Du, C., Zhou, X., Ma, J., Shi, J., Chen, A.B., Jiang, Z.& Chen, J. 2004, AJ, 128, 2265
Duffau, S., Zinn, R. & Vivas, A.K. 2006, ApJ, 636, L97
Eggen, O.J., Lynden-Bell, D. & Sandage, A.R. 1962, ApJ, 136, 748
Eisenstein, D.J., Annis, J., Gunn, J.E., et al 2001, AJ, 122, 2267
Eisenstein, D.J., Liebert, J., Harris, H.C., et al. 2006, ApJS, 167, 40
Fan, X. 1999, AJ, 117, 2528
Feltzing, S. 2006, Mem.S.A.It., 77, 1103 (also astro-ph/0611118)
Finlator, K., Ivezić, Ž., Fan, X., et al 2000, AJ, 120, 2615
Flaugher, B. & Dark Energy Survey Collaboration, 2007, BAAS, 209, 22.01
Freeman, K. & Bland-Hawthorn, J. 2002, ARA&A, 40, 487
Fuhrmann, K. 2004, AN, 325, 3
Fukugita, M., Ichikawa, T., Gunn, J.E., Doi, M., Shimasaku, K., & Schneider, D.P. 1996, AJ, 111, 1748
Gilmore, G. & Reid, N. 1983, MNRAS, 202, 1025
Gilmore, G. & Wyse, R.F.G. 1985, AJ, 90, 2015
Gilmore, G., Wyse, R.F.G., Jones, J.B. 1995, AJ, 109, 1095
Gilmore, G., Wyse, R.F.G. & Kuijken, K. 1989, Annual review of astronomy and astrophysics. Volume 27, pp. 555-627.
Gilmore, G., Wyse, R.F.G., Norris, J.E. 2002, ApJ, 574, L39
Girard, T.M., Korchagin, V.I., Caseti-Dinescu, D.I., van Altena, W.F., López, C.E. & Monet, D.G. 2006, AJ, 132, 1768
Girardi, L. & Salaris, M. 2001, MNRAS, 323, 109
Girardi, L., Grebel, E.K., Odenkirchen, M. & Chiosi, C. 2004, A&A, 422, 205
Grillmair, C.J. 2006a, ApJ, 645, L37
Grillmair, C.J. 2006b, ApJ, 651, L29
Gunn, J.E., Knapp, G.R. & Tremaine, S.D. 1979, AJ, 84, 1181
Gunn, J.E., Carr, M., Rockosi, C., et al. 1998, AJ, 116, 3040
Gunn, J.E., Siegmund, W.A., Mannery, E.J., et al. 2006, AJ, 131, 2332
Harris, W.E. 1996, AJ, 112, 1487
Helmi, A., Ivezić, Ž., Prada, F., et al. 2003, ApJ, 586, 195
Helmi, A., White, S.D.M., de Zeeuw, P.T. & Zhao, H. 1999, Nature, 402, 53
Hesser, J.E., Harris, W.E., Vandenberg, D.A., et al. 1987, PASP, 99, 739
Hogg, D.W., Finkbeiner, D.P., Schlegel, D.J. & Gunn, J.E. 2002, AJ, 122, 2129
Holberg, J.B. & Bergeron, P. 2006, AJ, 132, 1221
Ivezić, Ž., Goldston, J., Finlator, K., et al. 2000, AJ, 120, 963
Ivezić, Ž., Lupton, R.H., Anderson, S., et al. 2003, Proceedings of the Workshop *Variability with Wide Field Imagers*, Mem. Soc. Ast. It., 74, 978 (also astro-ph/0301400)
Ivezić, Ž, Lupton, R.H., Schlegel, D., et al. 2004, AN, 325, 583
Ivezić, Ž., Bond, N., Jurić, M., et al. 2005, ASP Conference Series, Vol. 338, Proceedings of a meeting held 18-20 October 2004 at Lowell Observatory, Flagstaff, Arizona, USA. Edited by P. Kenneth Seidelmann and Alice K. B. Monet. San Francisco: Astronomical Society of the Pacific, 2005., p.201 (also astro-ph/0701502)
Ivezić, Ž., Smith, J. A., Miknaitis, G., et al. 2006a, astro-ph/0701508
Ivezić, Ž., Schlegel, D., Uomoto, A., et al. 2006b, Mem. Soc. Ast. It., 77, 1057
Ivezić, Ž., Smith, J. A., Miknaitis, G., et al. 2007, AJ, 134, 973
Ivezić, Ž., Sesar, B., Jurić, M. et al. 2008, ApJ, 684, 287 (I08)
Jackson, T., Ivezić, Ž. & Knapp, G.R. 2002, MNRAS, 337, 749
Jurić, M., Ivezić, Ž., Brooks, A., et al. 2008, ApJ, 673, 864 (J08)
Jorgensen, B.R. & Lindegren, L. 2005, A&A, 436, 127
Kaczmarczik, M.C., Richards, G.T. & Schlegel, D. 2007, BAAS, Vol. 39, p.798
Kaiser, N., Aussel, It., Burke, B.E., et al. 2002, in "Survey and Other Telescope Technologies and Discoveries", Tyson, J.A. & Wolff, S., eds. Proceedings of the SPIE, 4836, 154
Karaali, S., Bilir, S. & Tuncel, S. 2005, PASA, 22, 24
Keller, S.C., Schmidt, B.P., Bessell, M.S., et al. 2007, astro-ph/0702511
Kurucz, R.L. 1979, ApJS, 40, 1
Laird, J.B., Carney, B.W. & Latham, D.W. 1988, AJ, 95, 1843
Lee, Y.S., Beers, T.C., Sivarani, T., et al. 2007a, submitted to AJ
Lee, Y.S., Beers, T.C., Sivarani, T., et al. 2007b, submitted to AJ

Lenz, D.D., Newberg, J., Rosner, R., Richards, G.T., Stoughton, C. 1998, ApJS, 119, 121
Lupton, R.H. 1993, *Statistics in Theory and Practice*, Princeton University Press, Princeton, New Jersey
Lupton, R.H., Ivezić, Ž., Gunn, J.E., Knapp, G.R., Strauss, M.A. & Yasuda, N. 2002, in "Survey and Other Telescope Technologies and Discoveries", Tyson, J.A. & Wolff, S., eds. Proceedings of the SPIE, 4836, 350
Majewski, S.R. 1992, ApJS, 78, 87
Majewski, S.R. 1993, ARA&A, 31, 575
Majewski, S.R., Skrutskie, M.F., Weinberg, M.D. & Ostheimer, J.C. 2003, ApJ, 599, 1082
Mannery, E.J. & Wallerstein, G. 1971, AJ, 76, 9
Martin, N.F., Irwin, M.J., Ibata, R.A., et al. 2006, MNRAS, 367, L69
Morrison, H.L., Flynn, C. & Freeman, K.C. 1990, 100, 1191
Munn, J.A., Monet, D.G., Levine, S.E., et al. 2004, AJ, 127, 3034
Munn, J.A., Monet, D.G., Levine, S.E., et al. 2008, AJ, 136, 895
Newberg H.J., Yanny, B., Rockosi, C., et al. 2002, ApJ, 569, 245
Nordström, B., Mayor, M., Andersen, J., et al. 2004, A&A, 418, 989
Norris, J. 1987, ApJ, 314, L39
Ojha, D.K., Bienayme, O., Robin, A.C., Creze, M. & Mohan, V. 1996, A&A, 311, 456
Pagel, B.E.J. & Patchett, B.E. 1975, MNRAS, 172, 13
Penarrubia, J., Martinez-Delgado, D., Rix, H.W., et al. 2005, ApJ, 626, 128
Perryman, M.A.C., de Boer, K.S., Gilmore, G., et al. 2001; A&A, 369, 339
Pickles, A.J. 1998, PASP, 110, 863
Pier, J.R., Munn, J.A., Hindsley, R.B., Hennesy, G.S., Kent, S.M., Lupton, R.H. & Ivezić, Ž. 2003, AJ, 125, 1559
Pourbaix, D., Knapp, G.R., Szkody, P., et al. 2005, A&A, 444, 643
Ramírez, I & Meléndez, J. 2005, ApJ, 626, 465
Ramírez, I., Allende Prieto, C. & Lambert, D.L. 2007, A&A, 465, 271
Reddy, B.E., Lambert, D.L. & Allende Prieto, C. 2006, MNRAS, 367, 1329
Reid, I.N., van Wyk, F., Marang, F., et al. 2001, MNRAS, 325, 931
Reid, I.N., Gizis, J.E. & Hawley, S.L. 2002, AJ, 124, 2721
Richards, G., Fan, X., Newberg, H., et al. 2002, AJ, 123, 2945
Robin, A.C., Reylé, C., Derriére, S. & Picaud, S. 2003, A&A, 409, 523
Ryan, S.G. & Norris, J.E. 1991, AJ, 101, 1835
Sandage, A. 1969, ApJ, 158, 1115
Sandage, A. & Smith, L.L. 1963, ApJ, 137, 1057
Schlegel, D., Finkbeiner,D.P. & Davis, M. 1998, ApJ500, 525
Schneider, D. P., Hall, P. B., Richards, G. T. et al. 2007, accepted to AJ
Schwarzschild, M., Searle, L. & Howard, R. 1955, ApJ, 122, 353
Scranton, R., Johnston, D., et al. 2002, ApJ, 579, 48
Sesar, B., Ivezić, Ž., Lupton, R.H., et al. 2007, AJ, 134, 2236
Sekiguchi, M. & Fukugita, M. 2000, AJ, 120, 1072
Siegel, M.H., Majewski, S.R., Reid, I.N., & Thompson, I.B. 2002, ApJ, 578, 151
Simones, J., Newberg, H.J. & Cole, N. 2008, BAAS (AAS Meeting #211)
Skrutskie, M.F., Cutri, R.M., Stiening, R., et al. 2006, AJ, 131, 1163
Smith, J.A., Tucker, D.L., Kent, S.M., et al. 2002, AJ, 123, 2121
Smolčić, V., Ivezić, Ž, Knapp, G.R., et al. 2004, ApJ, 615, L141
Snider, S., Allende Prieto, C., von Hippel, T. Beers, T.C., Sneden, C., Qu, Y. & Rossi, S. 2001, ApJ, 562, 528
Springel, V. & Hernquist, L. 2003, MNRAS, 339, 312
Stoughton, C., Lupton, R.H., Bernardi, M., et al. 2002, AJ, 123, 485
Strauss, M.A., Weinberg, D.H., Lupton, R.H., et al. 2002, AJ 124, 1810
Strömgren, B. 1966, ARA&A, 4, 433
Tinsley, B.M. 1975, ApJ, 197, 159
Tucker, D., Kent, S., Richmond, M.W., et al. 2006, AN, 327, 821
Tyson, J.A. 2002, in *Survey and Other Telescope Technologies and Discoveries*, Tyson, J.A. & Wolff, S., eds. Proceedings of the SPIE, 4836, 10
VandenBerg, D.A. & Clem, J.L. 2003, AJ, 126, 778
Vivas, A.K., Zinn, R., Andrews, P., *et al.* 2001, ApJ, 554, L33
Vivas, A.K. & Zinn, R. 2006, AJ, 132, 714
Wallerstein, G. 1962, ApJS, 6, 407
Weinberg, M.D. 1992, ApJ, 384, 81
Wilkinson, M.I., Vallenari, A., Turon, C., et al. 2005, MNRAS, 359, 1306
Wyse, R.F.G. & Gilmore, G. 1995, AJ, 110, 2771
Wyse, R.F.G. 2006, Mem.S.A.It., 77, 1036
Yanny, B., Newberg, H. J., Kent, S., et al. 2000, ApJ, 540, 825
York, D.G., Adelman, J., Anderson, S., et al. 2000, AJ, 120, 1579

TABLE 1
BEST-FIT PARAMETERS[a] FOR THE DISK VELOCITY DISTRIBUTION[b].

Quantity	a	b	c
$\bar{v_\phi}^1$	-194	19.2	1.25
σ_ϕ^1	12	1.8	2.0
σ_ϕ^2	34	1.2	2.0
σ_ϕ^D	30	3.0	2.0
σ_R	40	5.0	1.5
σ_Z	25	4.0	1.5

[a] All listed quantities are modeled as $a + b|Z|^c$, with Z and R in kpc, and velocities in km s^{-1}.

[b] The v_ϕ distribution is non-gaussian, and can be formally described by a sum of two gaussians with a fixed normalization ratio f_k:1, with $f_k = 3$. The mean value for the second gaussian has a fixed offset from the first gaussian, $\bar{v_\phi}^2 = (\bar{v_\phi}^1 - \Delta \bar{v_\phi})$, with $\Delta \bar{v_\phi} = 34$ km/s. When $\bar{v_\phi}^1 > 0$ (at $Z \sim 6$ kpc), $\bar{v_\phi}^1$ should be set to 0. The velocity dispersion for the second gaussian is given by σ_ϕ^2. If this non-gaussianity is ignored, the dispersion is given by σ_ϕ^D.
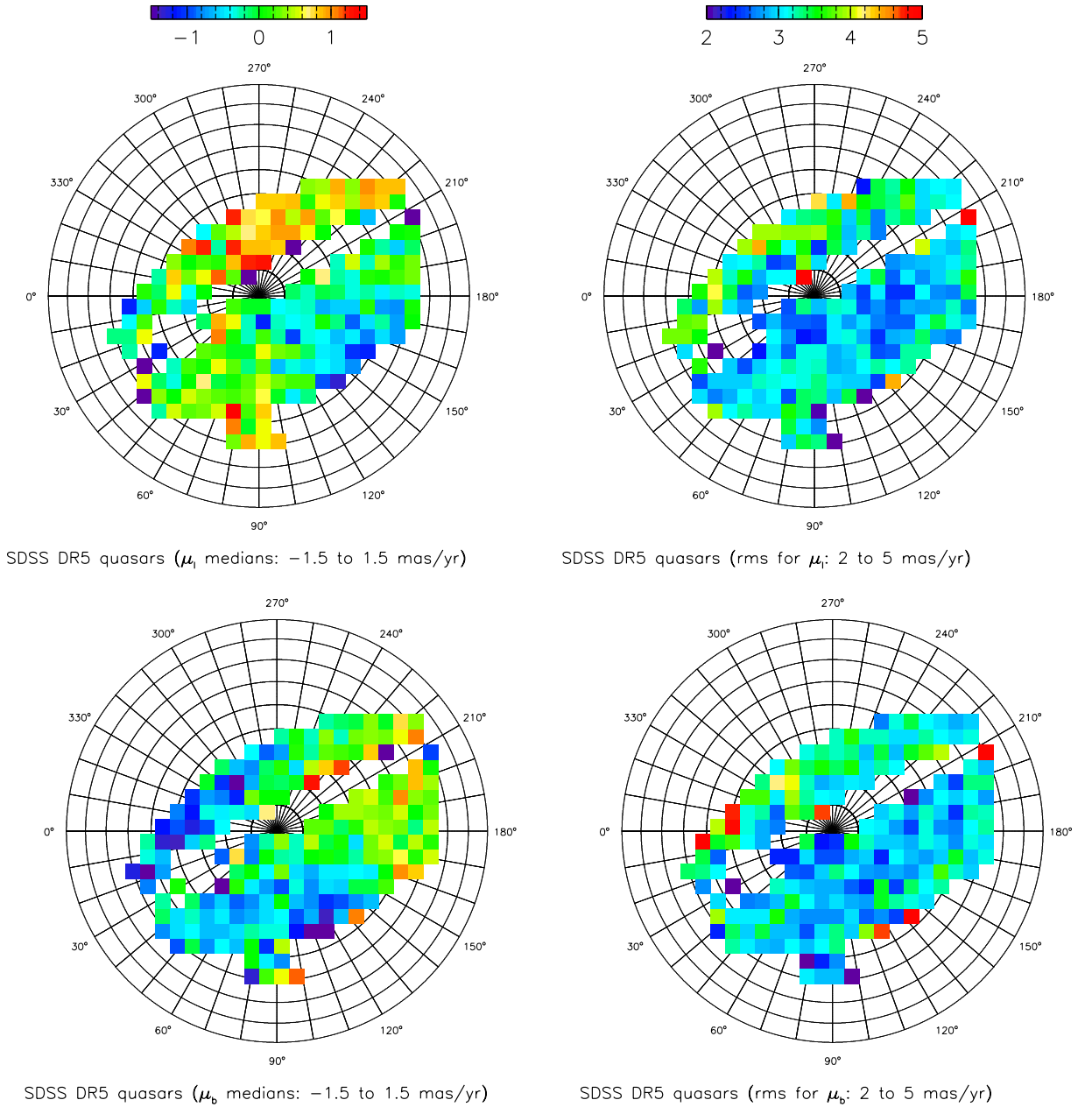
FIG. A1.— The behavior of proper motion measurements for 47,000 spectroscopically confirmed SDSS quasars with galactic latitude $b > 0$. The color-coded maps (see the legend on top, units are mas/yr) show the distribution of the median (left) and rms (right) for longitudinal (top) and latitudinal (bottom) proper motion components in Lambert projection of the northern Galactic cap. For both components, the distribution width for the medians is 0.65 mas/yr (after accounting for statistical noise, the implied scatter of systematic proper motion errors across the sky is 0.60 mas/yr). The median proper motion for the full quasar sample is 0.15 mas/yr in the longitudinal direction, and -0.20 mas/yr in the latitudinal direction.
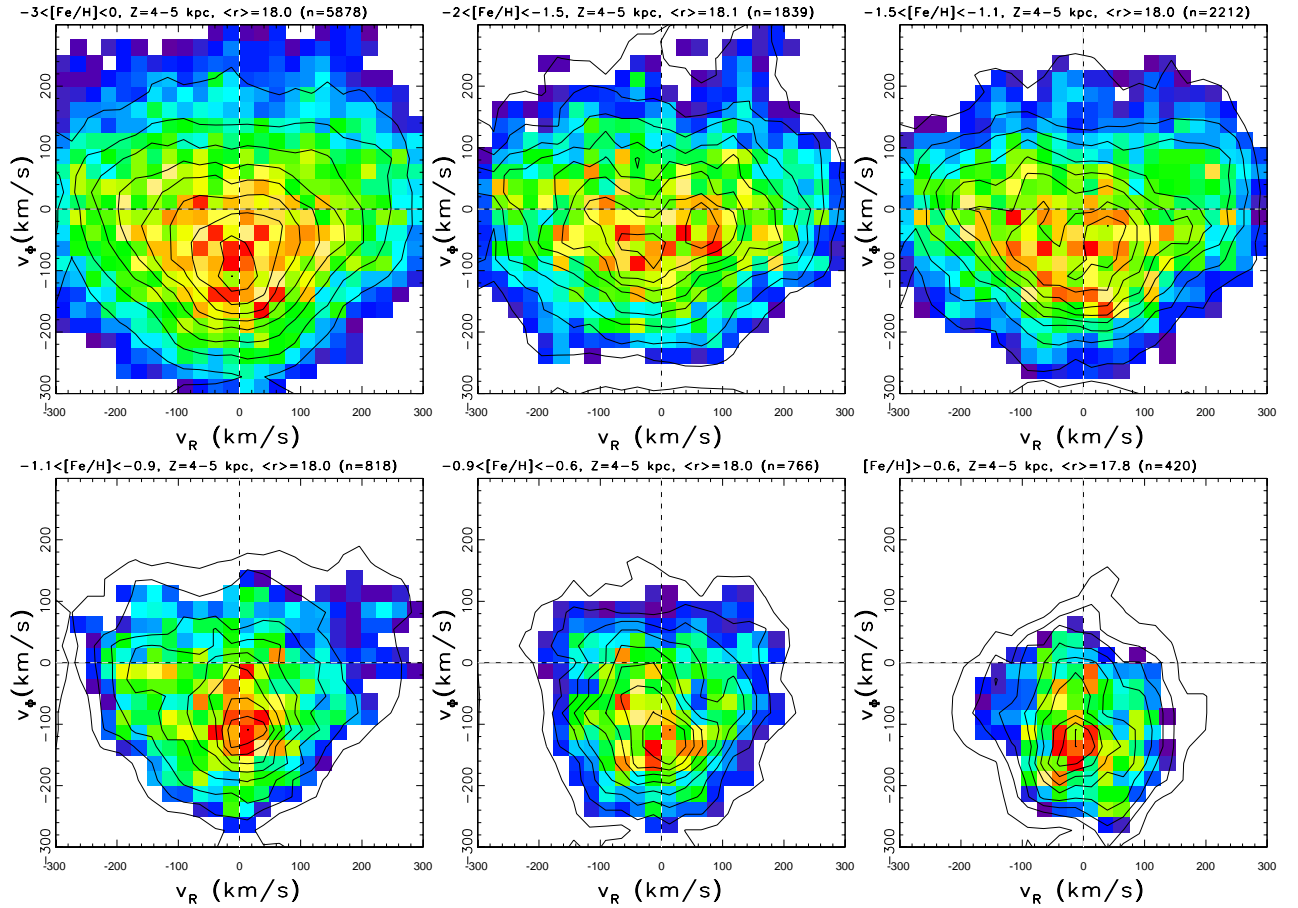
FIG. A2.— The change of the v_Φ vs. v_R velocity distribution with metallicity, at a nearly constant R and Z. The top left panel shows the v_Φ vs. v_R diagram for ∼6,000 blue ($0.2 < g - r < 0.4$) stars from the $Z = 4 - 5$ kpc range and detected towards the North Galactic pole ($b > 80°$). The distribution is shown using linearly-spaced contours, and with color-coded map showing counts in pixels (low to high from blue to red). Other five panels are analogous, and show subsamples selected by metallicity, with the $[Fe/H]$ range listed above each panel (also listed are the median r band magnitude and subsample size). The measurement errors are typically 70 km s^{-1}. Note the strong variation of median v_Φ with metallicity.
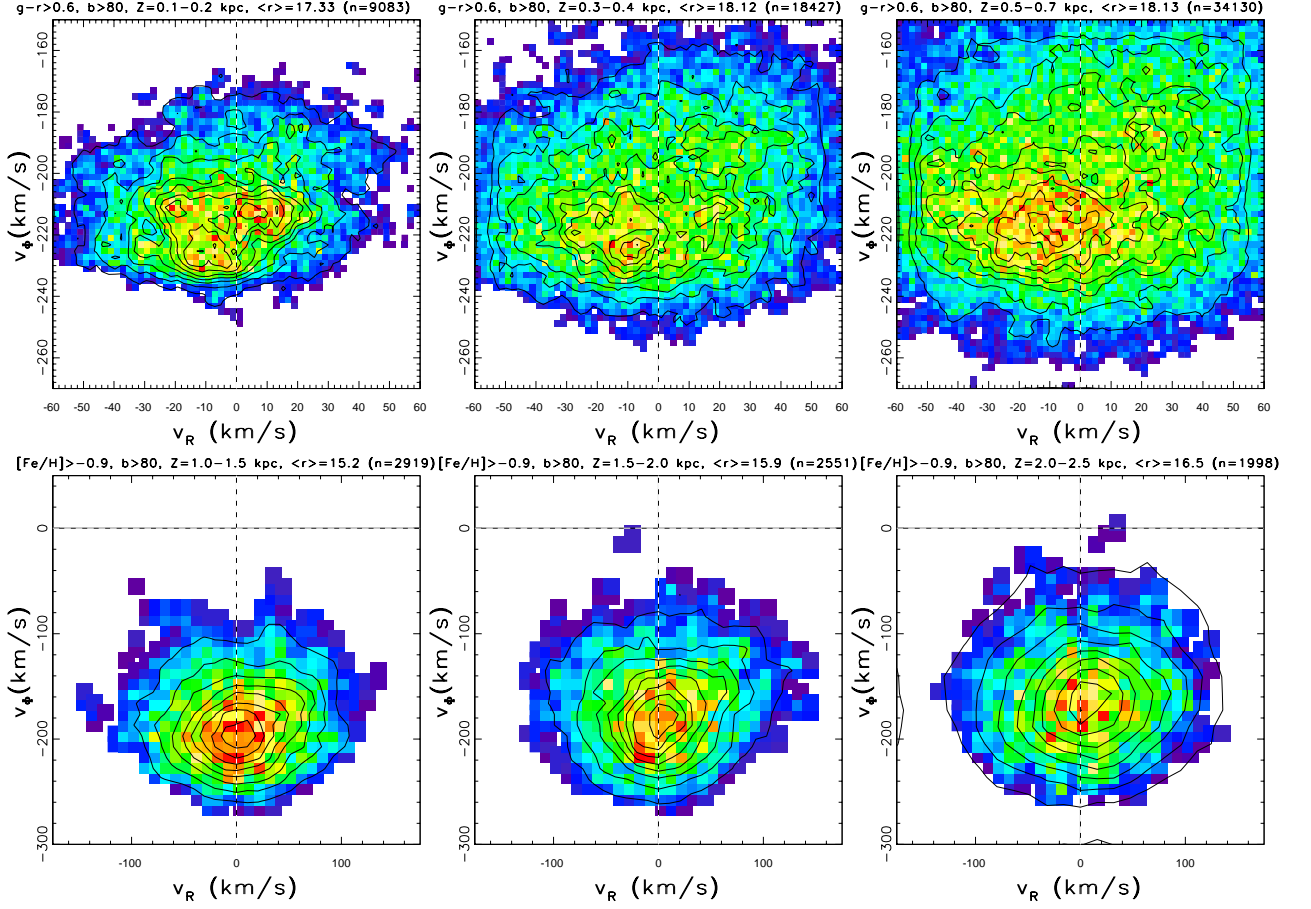
FIG. A3.— Similar to Figure A2, except that the v_Φ vs. v_R velocity distribution is studied as a function of Z. The top row shows the v_Φ vs. v_R diagrams for ~60,000 red ($g−r$ >0.6) stars from the $Z = 100−700$ pc range observed towards north galactic pole. Each panel corresponds to a narrow Z bin, with the range shown above each panel. The measurement errors vary from typically ~3 km s^{-1} in the closest bin to ~12 km s^{-1} in the most distant bin. Note the complex multi-modal substructure in the top left panel. The bottom three panels are analogous, and show the v_Φ vs. v_R diagrams for ~7,000 blue (0.2< $g−r$ <<0.4) stars with high metallicity ($[Fe/H] > −0.9$). The measurement errors vary from typically ~20 km s^{-1} in the closest bin to ~35 km s^{-1} in the most distant bin. Note that the median v_Φ becomes closer to zero as Z increases.
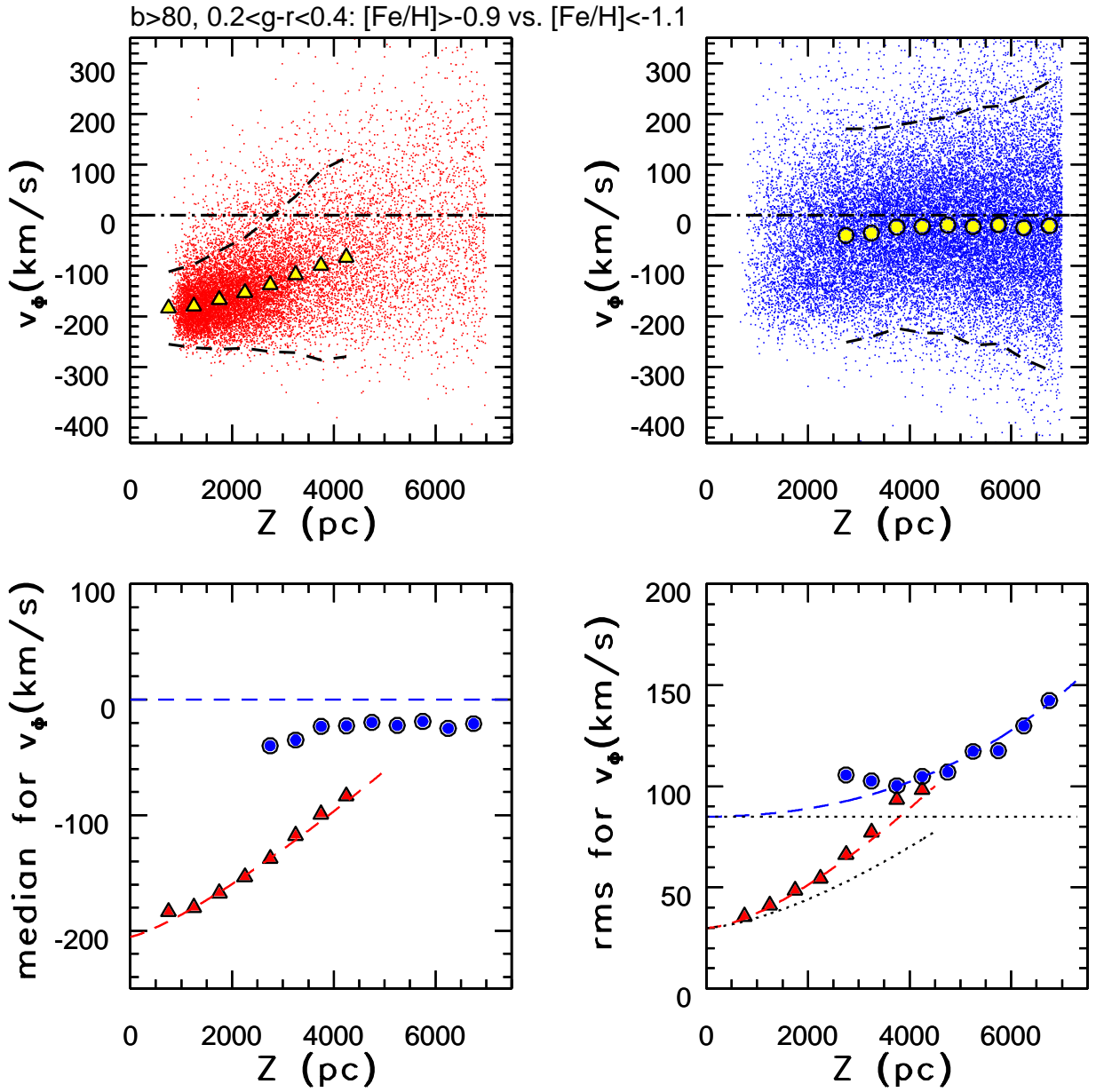
Fɪɢ. A4.— The dependence of the rotational velocity component, v_Φ, on the distance from the plane, for 14,000 high-metallicity ($[Fe/H] > -0.9$; top left panel) and 23,000 low-metallicity ($[Fe/H] < -1.1$, top right) stars with $b > 80°$. In the two top panels individual stars are shown by small dots, and the medians in bins of Z are shown by the large circles. The 2σ envelope around the medians is shown by dashed lines. The bottom two panels compare the medians (left) and dispersions (right) for the two subsamples shown in the top panels. The dashed lines in the bottom two panels show predictions of a kinematic model described in text. The dotted lines in the bottom right panel show model dispersions without a correction for the measurement errors.
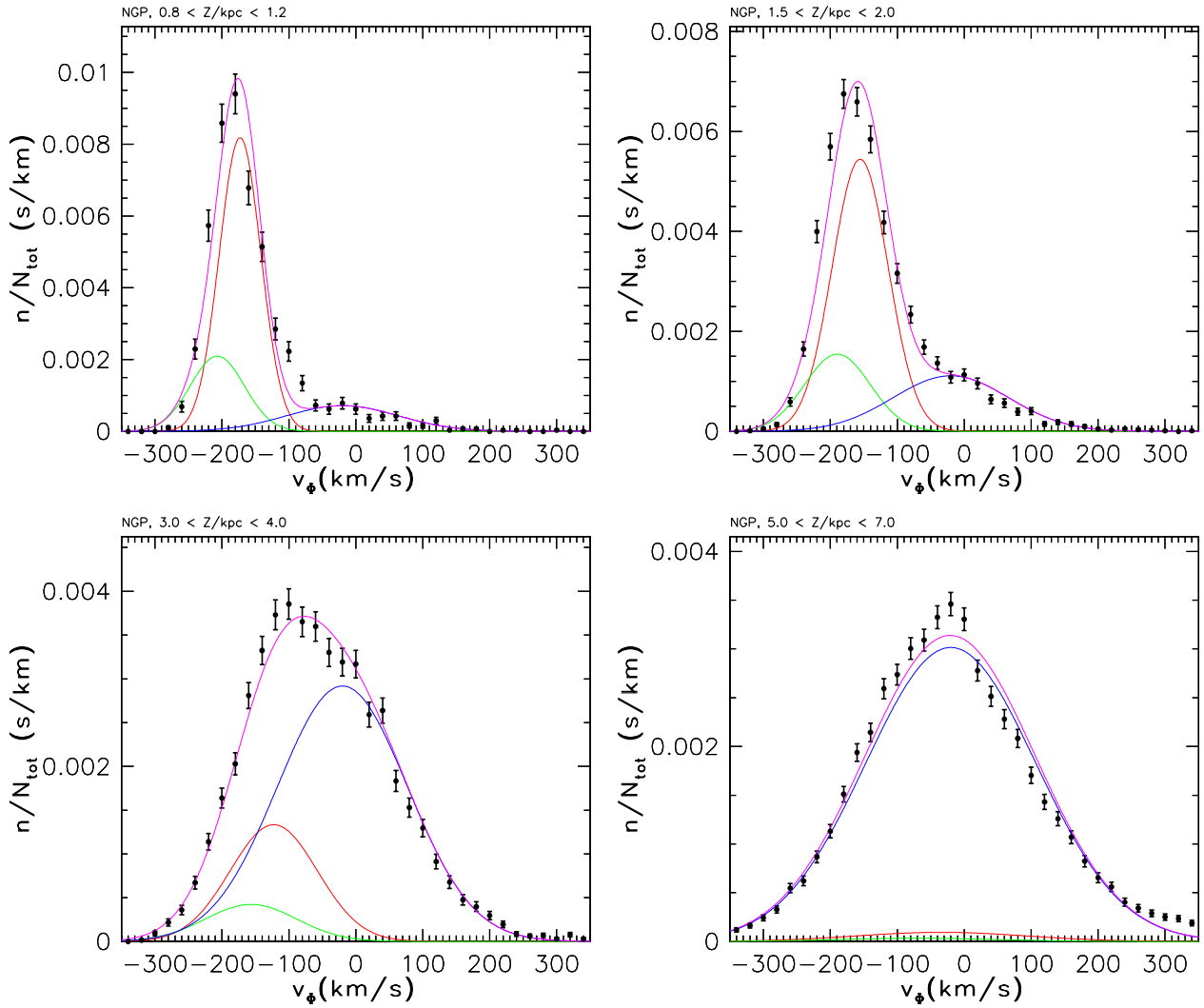
FIG. A5.— The symbols with error bars show measured rotational velocity distribution, v_Φ, for stars with $0.2 < g-r < 0.4$, $b > 80°$, and the distance from the galactic plane in the range in the range 0.8–1.2 kpc (top left, $\sim$1,500 stars), 1.5–2.0 kpc (top right, $\sim$4,100 stars), 3.0–4.0 kpc (bottom left, $\sim$6,400 stars) and 5.0–7.0 kpc (bottom right, $\sim$12,500 stars). The red and green curves show the contribution of a non-gaussian disk model (a sum of two gaussians with fixed, 1:3, relative normalization, see eqs. 19 and 20), the blue curves show a gaussian halo contribution, and the magenta curves are their sum.
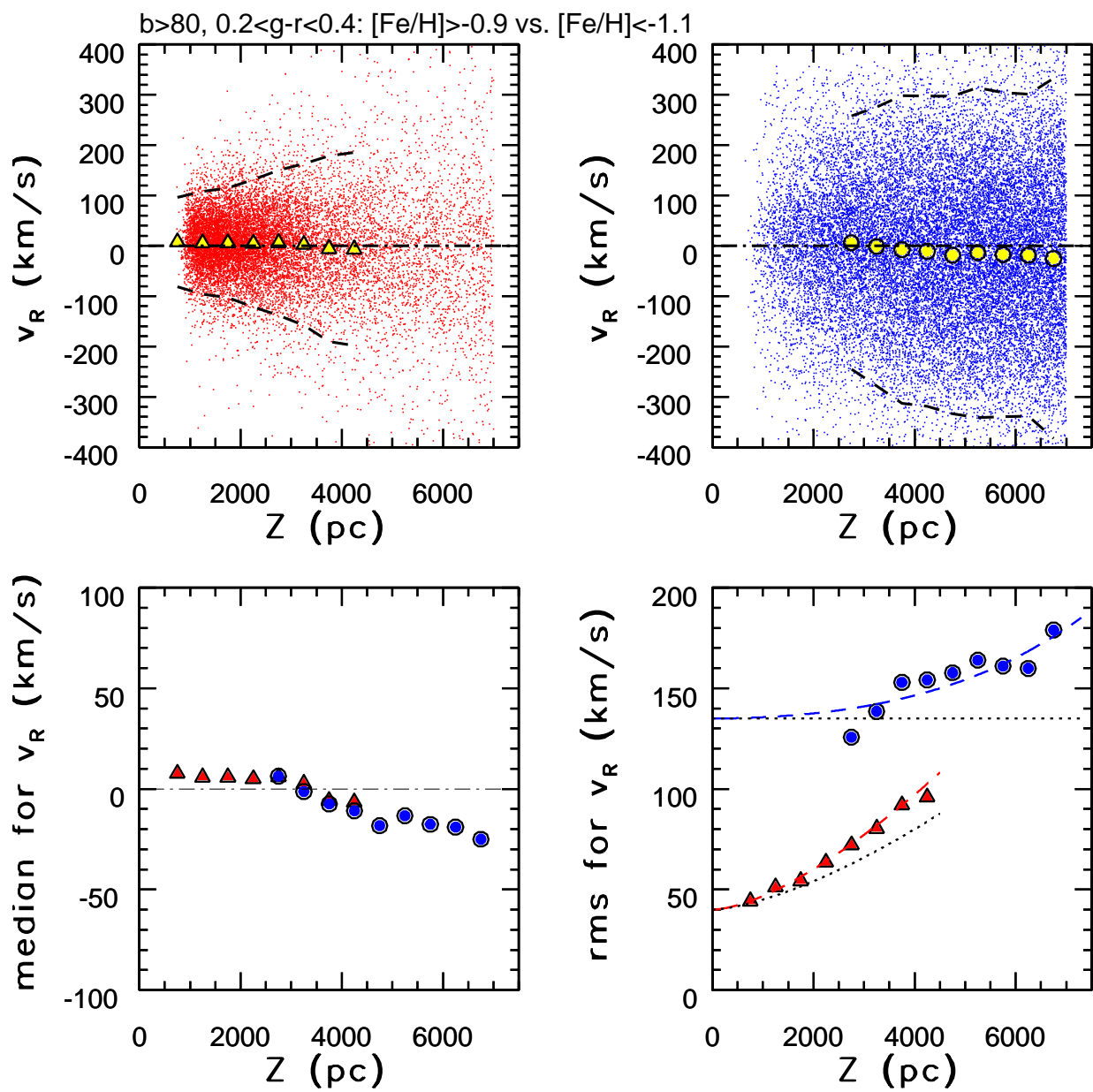
FIG. A6.— Analogous to Figure A4, except that the radial velocity component (*R*) is shown.
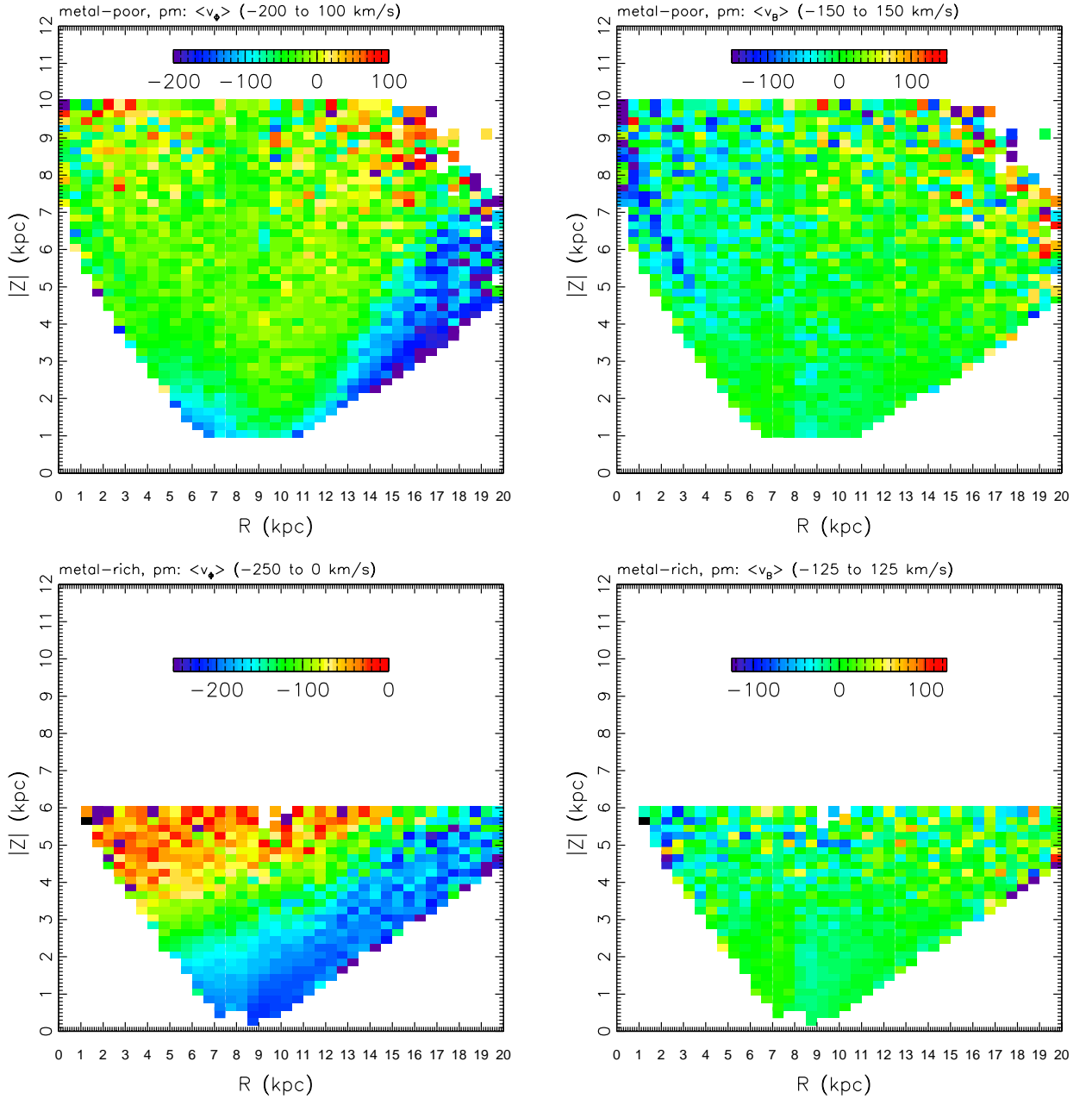
FIG. A7.— The dependence of velocity, measured using proper motions (left column: rotational component, v_Φ; right column: $v_B = \sin(b)v_R + \cos(b)v_Z$) on cylindrical galactocentric coordinates for blue ($0.2 < g - r < 0.4$) stars: 172,000 metal-poor halo-like stars ($[Fe/H] < -1.1$; top panels) and 205,000 metal-rich disk-like stars ($[Fe/H] > -0.9$; bottom panels), selected from three regions with $b > 80°$ (north galactic pole), $170° < l < 190°$ (anticenter), and $350° < l < 10°$ (center). The median values of velocity in each bin are color-coded according to the legend shown in each panel (km s^{-1}). The measurements are reliable at distances up to about 7 kpc. Regions beyond this limit are shown for halo stars for completeness. The fraction of disk stars is negligible at such distances, and their velocity distribution is shown for $Z < 6$ kpc. The region with negative velocity on the right side of top left panel is due to Monoceros stream. The thin region with negative velocity on the left side of top right panel is a data artefact.
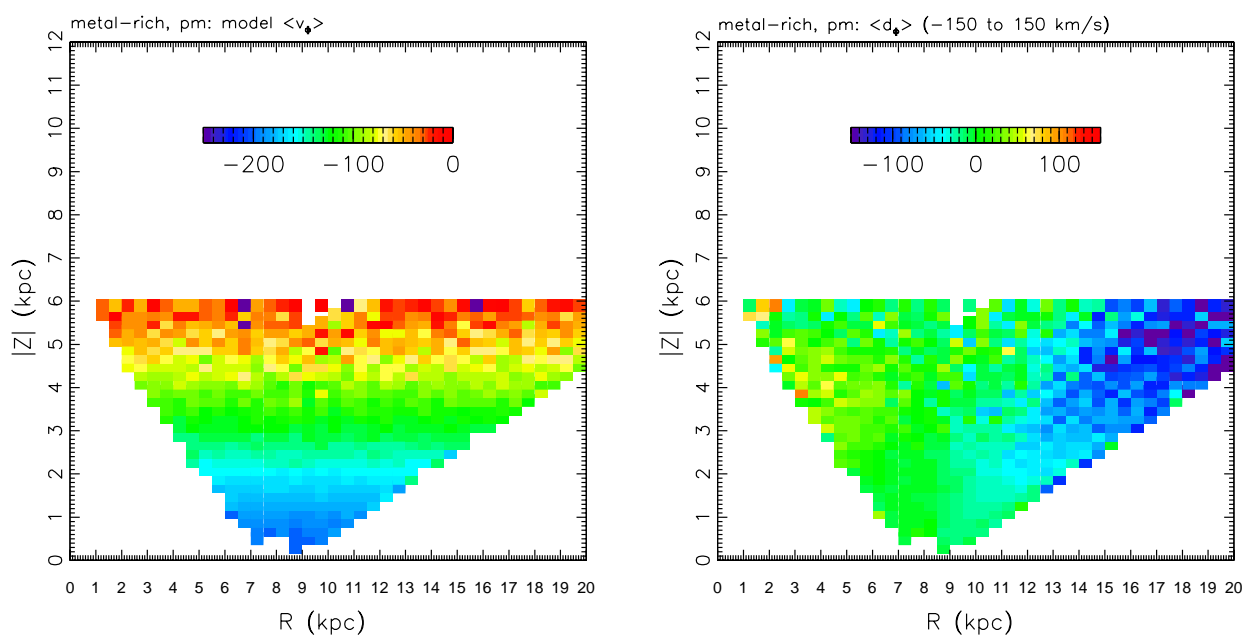
FIG. A8.— The left panel is analogous to the bottom left panel in Figure A7, except that here the median rotational velocity predicted by a model described in text is shown. The right panel shows the median difference between the data and model values. Large discrepancies at $R > 12$ kpc are due to Monoceros stream (at $R = 18$ kpc and $Z = 4$ kpc, disk stars rotate with a median $v_\phi \sim -100$ km s^{-1}, while for Monoceros stream $v_\phi \sim -200$ km s^{-1}).
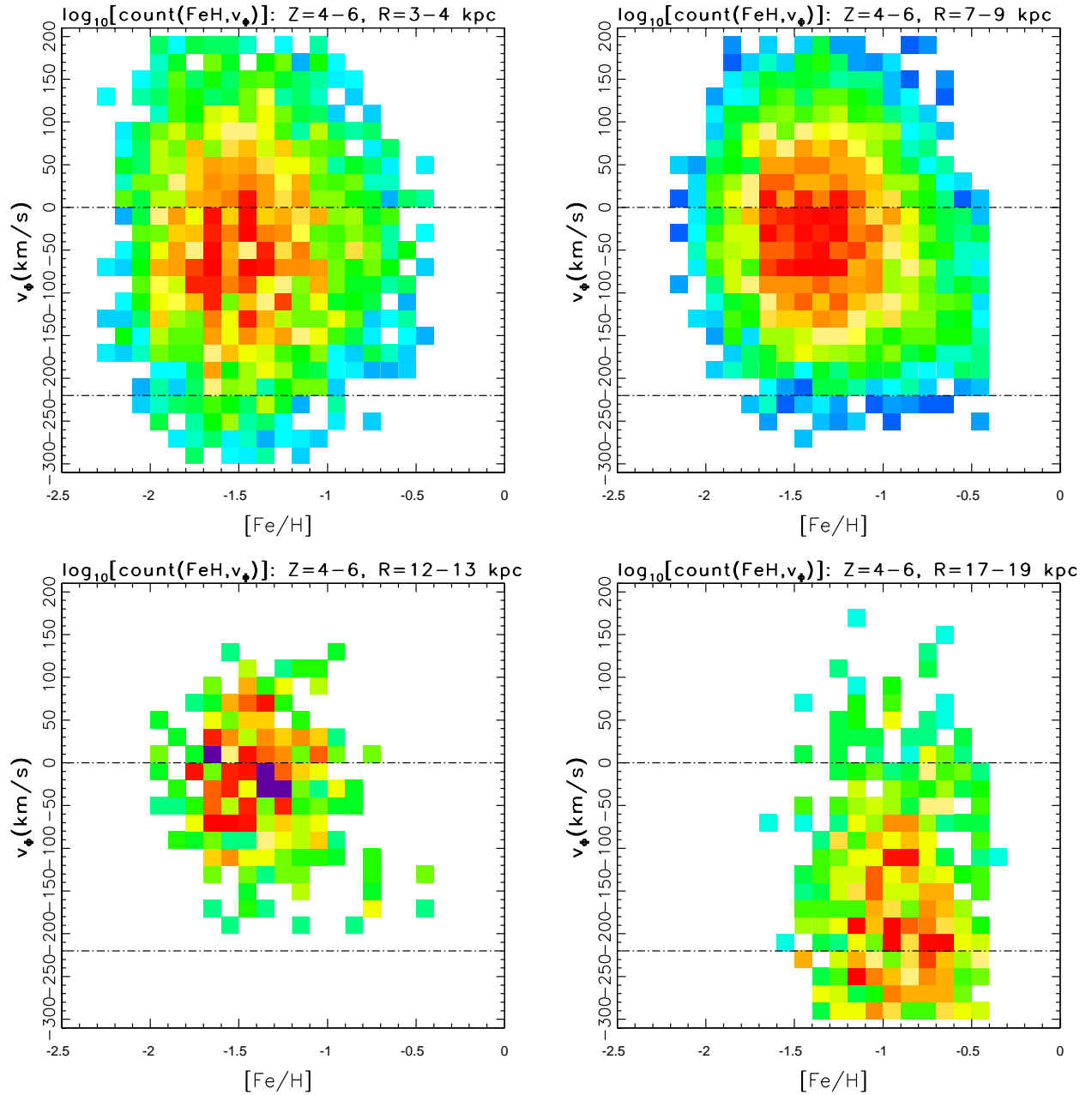
FIG. A9.— The distribution of stars with $0.2 < g - r < 0.4$ and distance from the galactic plane in the range $Z=4-6$ kpc in the rotational velocity vs. metallicity plane, for four ranges of galactocentric cylindrical radius, R (top left: 3–4 kpc; top right: 7–9 kpc; bottom left: 12–13 kpc; bottom right: 17–19 kpc). In each panel, the color-coded map shows the logarithm of counts in each pixel, scaled by the total number of stars. The horizontal lines at $v_\Phi = 0$ and $v_\Phi = -220$ km s^{-1} are added to guide the eye. High-metallicity ($[Fe/H] \sim -1$) stars with fast rotation ($v_\Phi \sim 220$ km s^{-1}) visible in the bottom right panel belong to the Monoceros stream, and are responsible for features seen at $R > 15$ kpc in the two left panels in Figure A7.
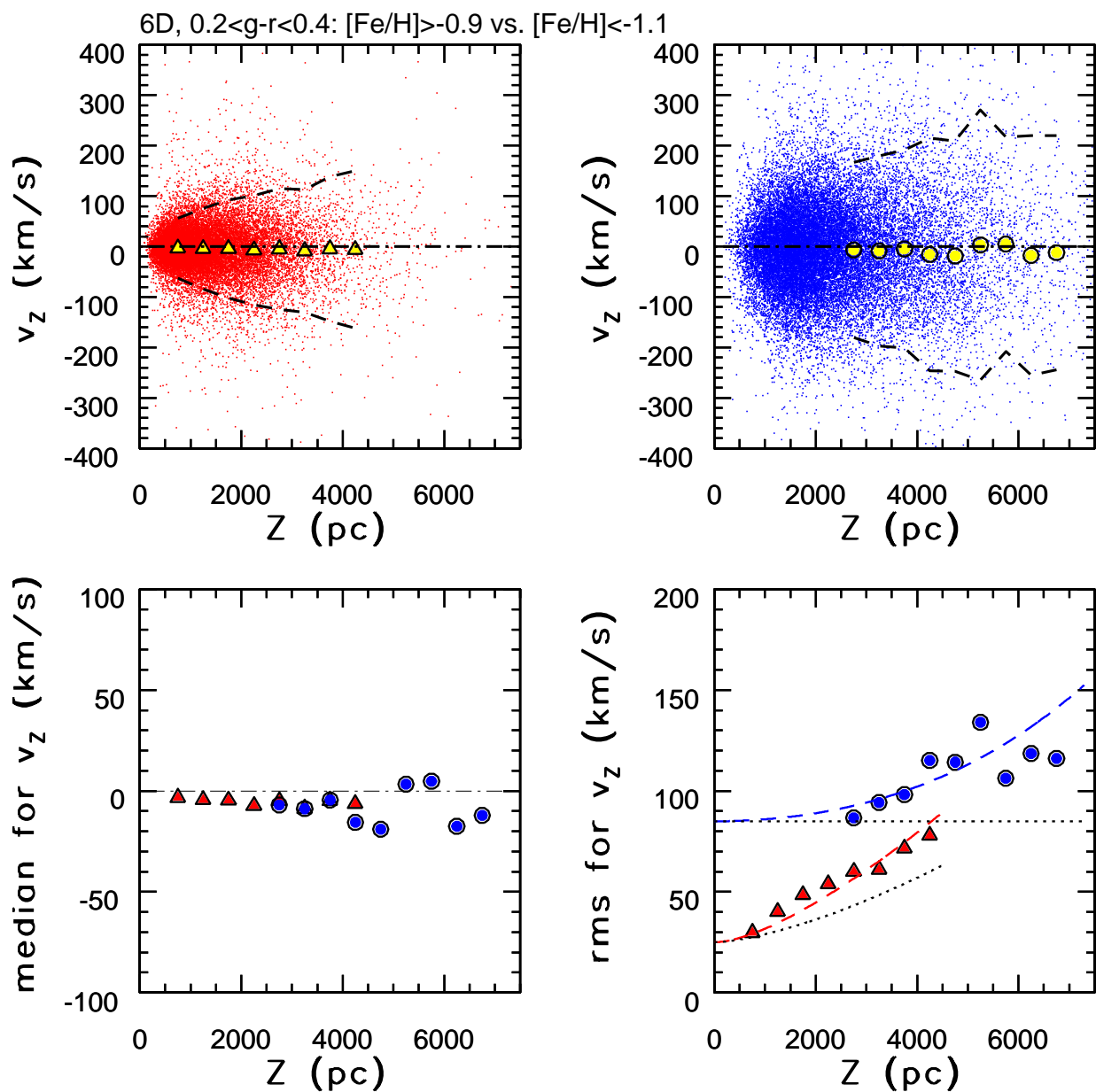
FIG. A10.— Similar to Figure A4, except that the vertical velocity component (Z) is shown, using a sample of stars with SDSS radial velocity measurements and $b > 0$ (20,000 stars in the high-metallicity subsample, and 6,000 stars in the low-metallicity sample). The behavior of rotational and radial velocity components for this sample is consistent with that shown in Figures A4 and A6, except for slight differences in measurement errors.
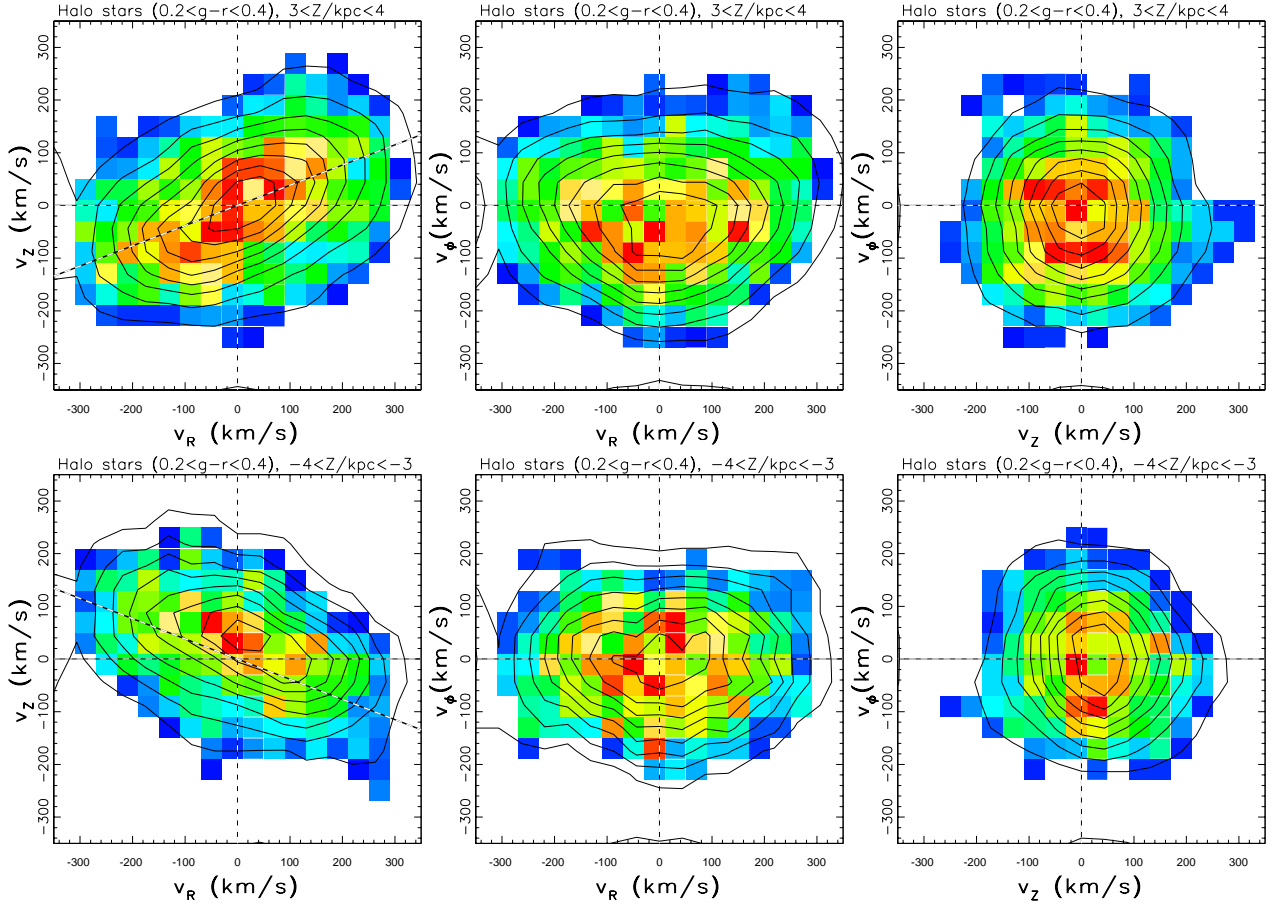
FIG. A11.— The three two-dimensional projections of the velocity distribution for two subsamples of candidate halo stars selected using spectroscopic metallicity ($-3 < [Fe/H] < -1.1$) and with $6 < R/\mathrm{kpc} < 11$. The top row corresponds to 2,000 stars with distances from the galactic plane $3 < Z/\mathrm{kpc} < 4$, and the bottom row to 1,200 stars with $-4 < Z/\mathrm{kpc} < -3$. The distributions are shown using linearly-spaced contours, and with color-coded map showing smoothed counts in pixels (low to high from blue to red). The measurement errors are typically 60 km s^{-1}. Note the strong evidence for velocity ellipsoid tilt in top and bottom left panels. The two dashed lines in these panels show median direction towards the Galactic center. Note also a non-vanishing median v_Z of ~ 15 km/s in the bottom left and right panels.
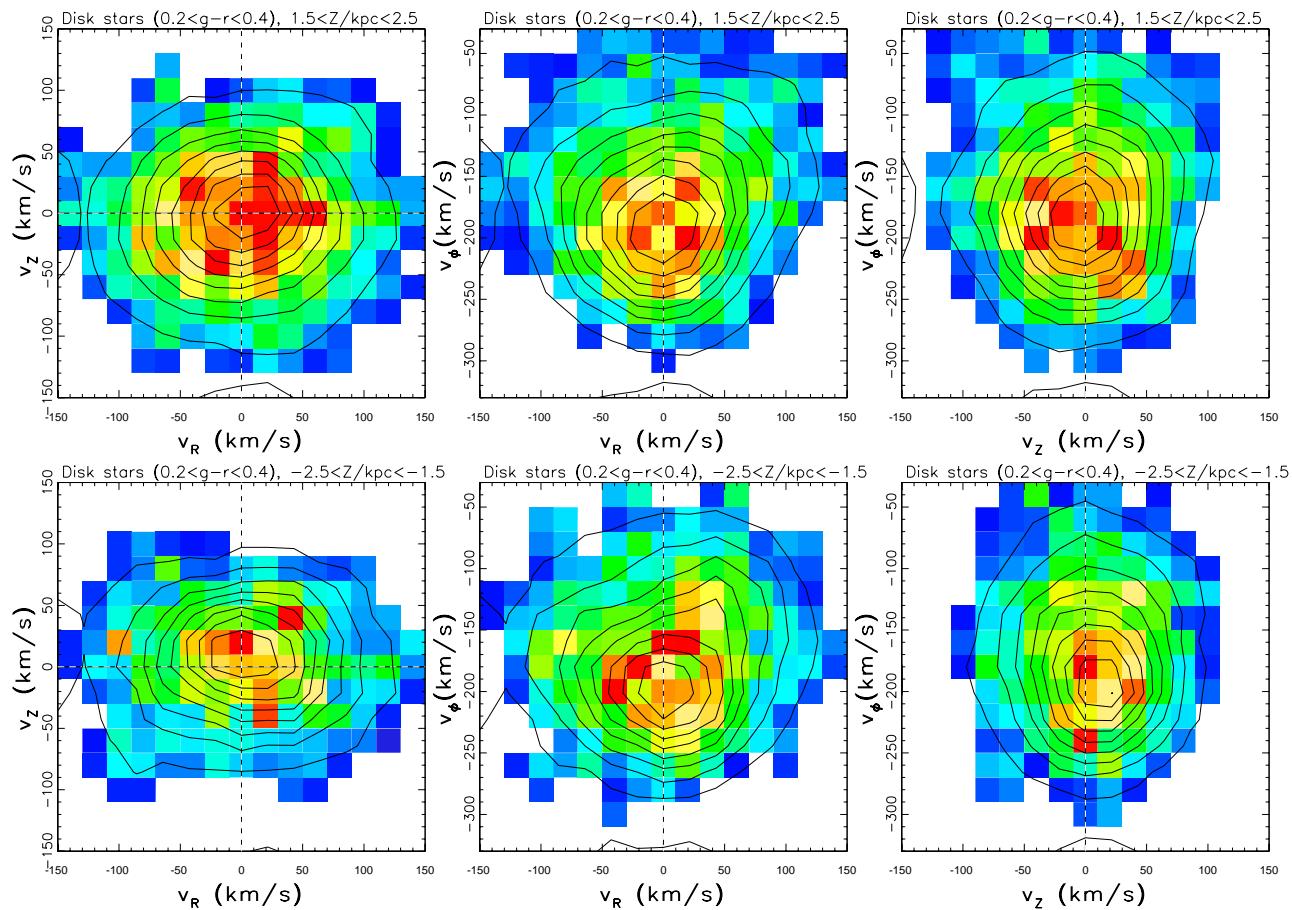
FIG. A12.— Analogous to Figure A11, except that the velocity distribution is shown for two subsamples of candidate disk stars selected using spectroscopic metallicity ($-0.9 < [Fe/H] < 1$). The top row corresponds to 1,700 stars with distances from the galactic plane $1.5 < Z/\text{kpc} < 2.5$, and the bottom row to 1,500 stars with $-2.5 < Z/\text{kpc} < -1.5$. The measurement errors are typically 35 km s^{-1}. Note the absence of velocity ellipsoid tilt in top and bottom left panels.
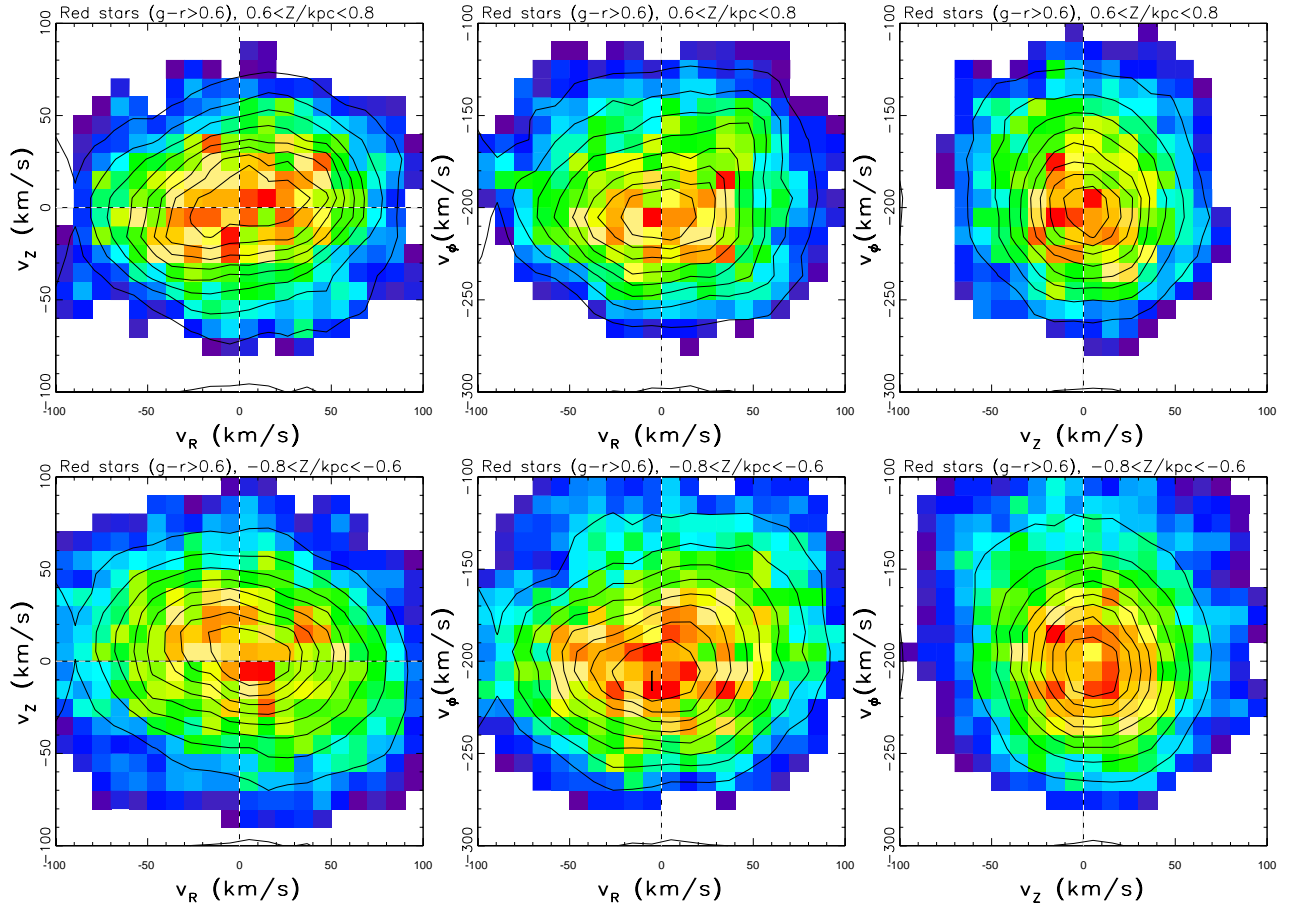
FIG. A13.— Analogous to Figure A12, except that the velocity distribution is shown for two subsamples of red stars ($g-r > 0.6$): the top row corresponds to 2,200 stars with distances from the galactic plane $0.6 < Z/\mathrm{kpc} < 0.8$, and the bottom row to 4,300 stars with $-0.8 < Z/\mathrm{kpc} < -0.6$. The measurement errors are typically 15 km s^{-1}.
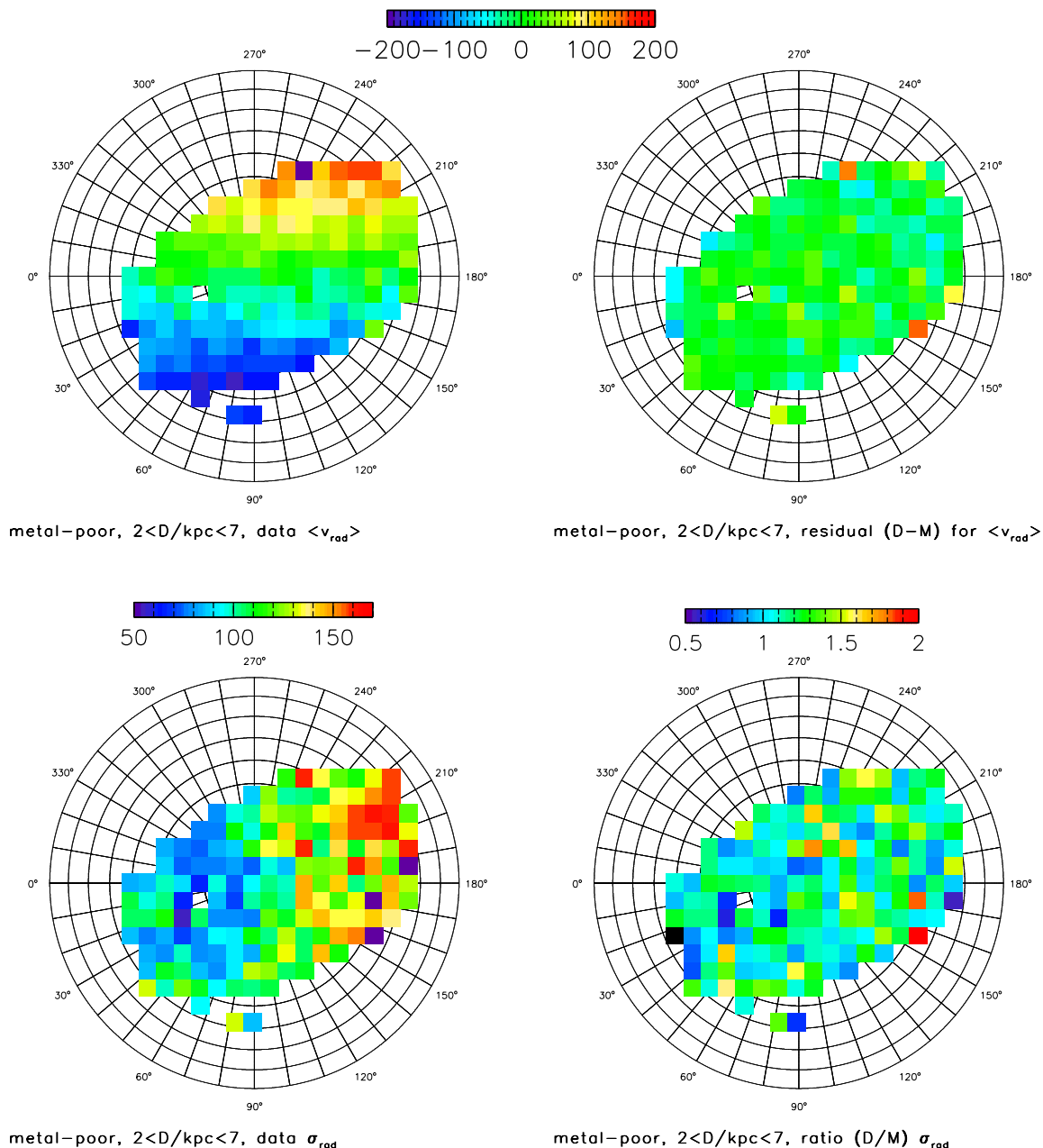
FIG. A14.— A comparison of medians and dispersions for measured and modeled radial velocity of blue ($0.2 < g-r < 0.4$) halo stars (spectroscopic $[Fe/H] < -1.1$) with distance in the range 2–7 kpc and $b > 0$. The top left panel shows median measured radial velocity color-coded according to the legend shown at the top (units are km s^{-1}). The top right panel shows the difference between this map and analogous map based on model-generated values of radial velocity, using the same scale as in the top left panel. The bottom left panel shows the dispersion of measured radial velocity color-coded according to the legend above it (units are km s^{-1}). The bottom right panel shows the ratio of this map and an analogous map based on model-generated values of radial velocity, color-coded according to the legend above it (dimensionless).
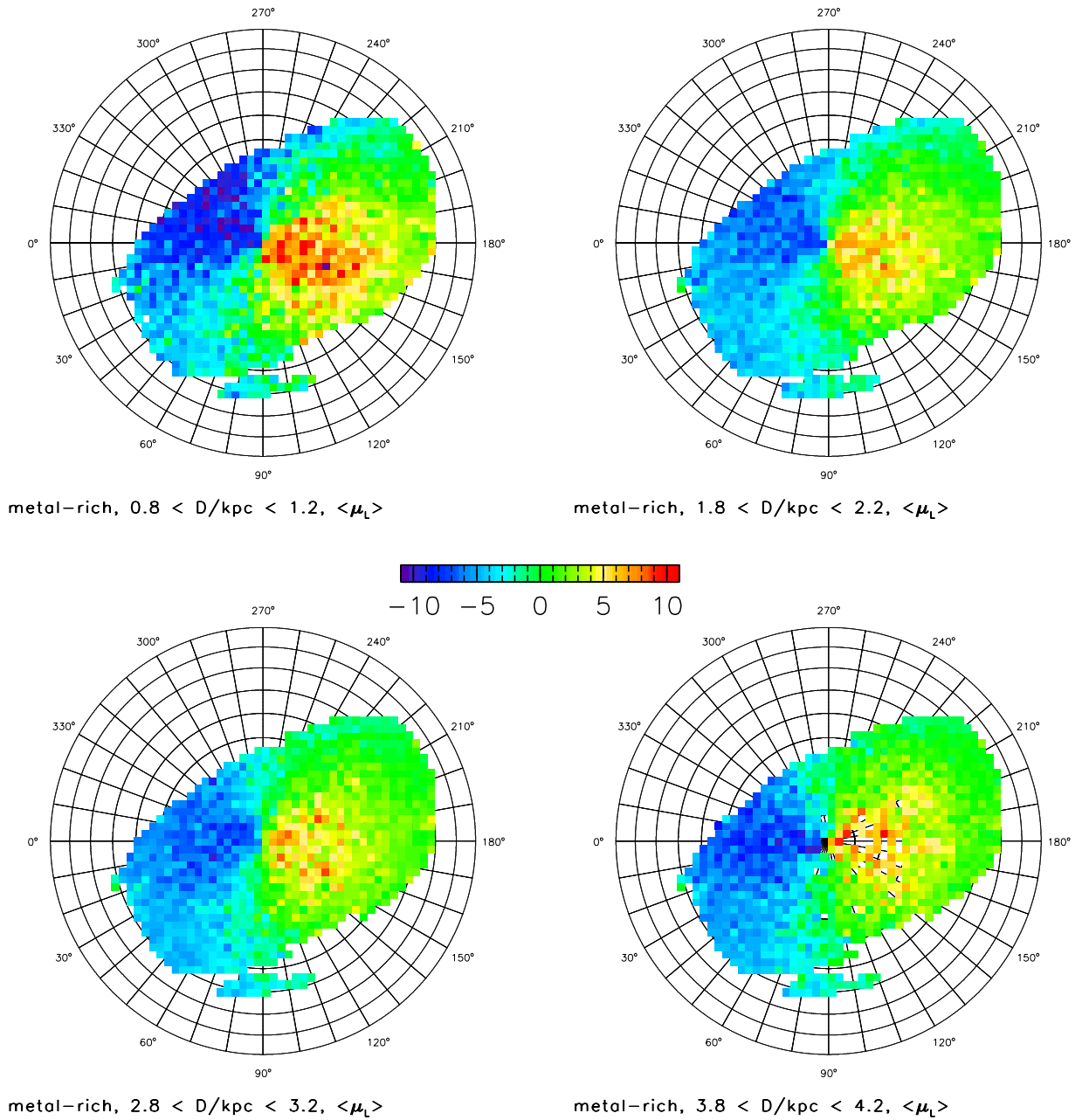
FIG. A15.— The distribution of the median longitudinal proper motion component in Lambert projection of the northern Galactic cap for high-metallicity ($[Fe/H] > -0.9$) blue ($0.2 < g-r < 0.4$) stars, in several distance bins (top left: 58,000 stars with D=0.8–1.2 kpc; top right: 119,000 stars with D=1.8–2.2 kpc; bottom left: 72,000 stars with D=2.8–3.2 kpc; bottom right: 43,000 stars with D=3.8–4.2 kpc). All maps are color-coded using the same scale, shown in the middle (units are mas/yr). Note that the magnitude of proper motion does not change appreciably as the distance varies from ~2 kpc to ~4 kpc. This is due to vertical gradient of the rotational velocity for disk stars (see Figure A3).
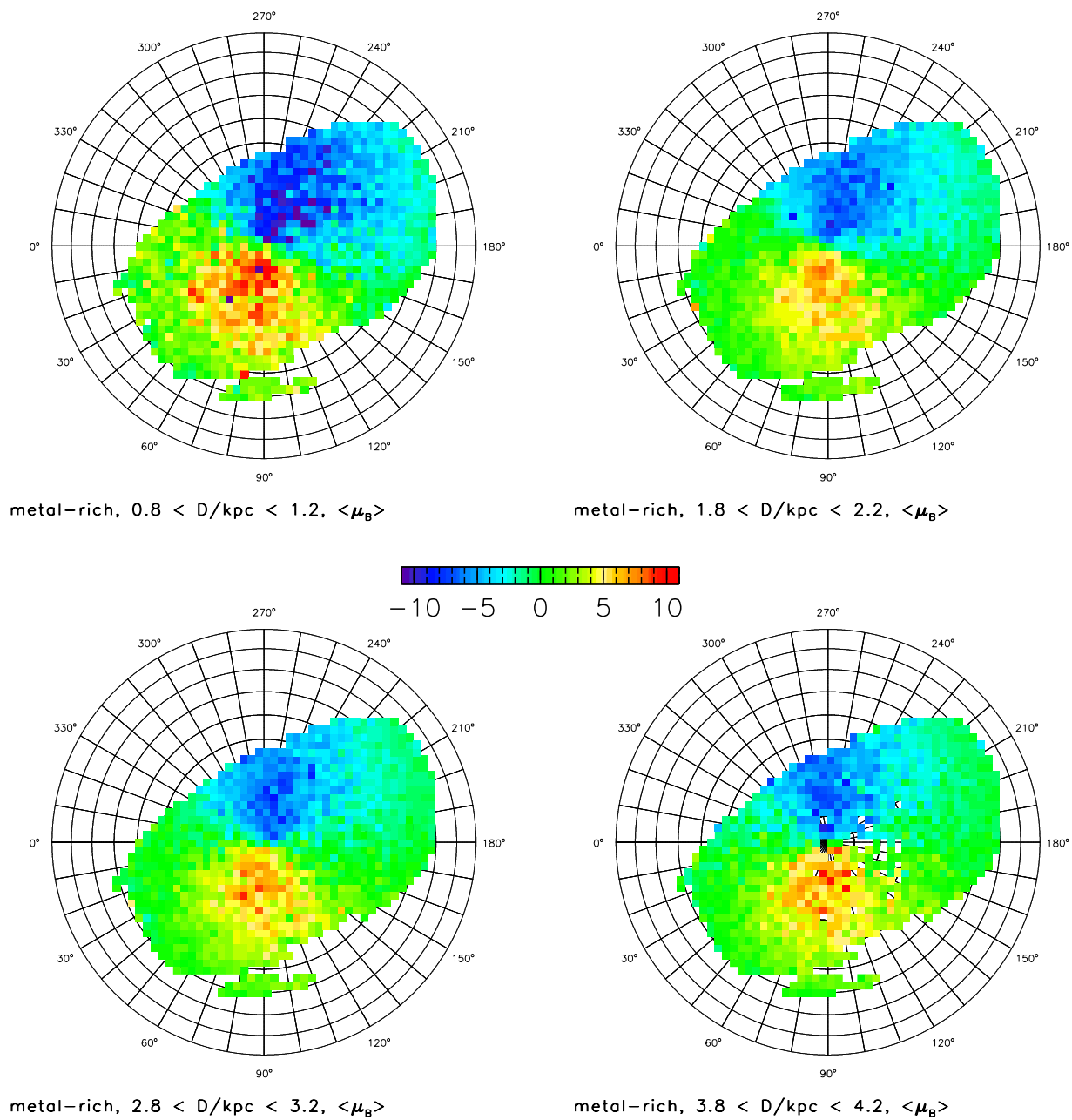
metal−rich, 0.8 < D/kpc < 1.2, <μ_B>

metal−rich, 1.8 < D/kpc < 2.2, <μ_B>

metal−rich, 2.8 < D/kpc < 3.2, <μ_B>

metal−rich, 3.8 < D/kpc < 4.2, <μ_B>

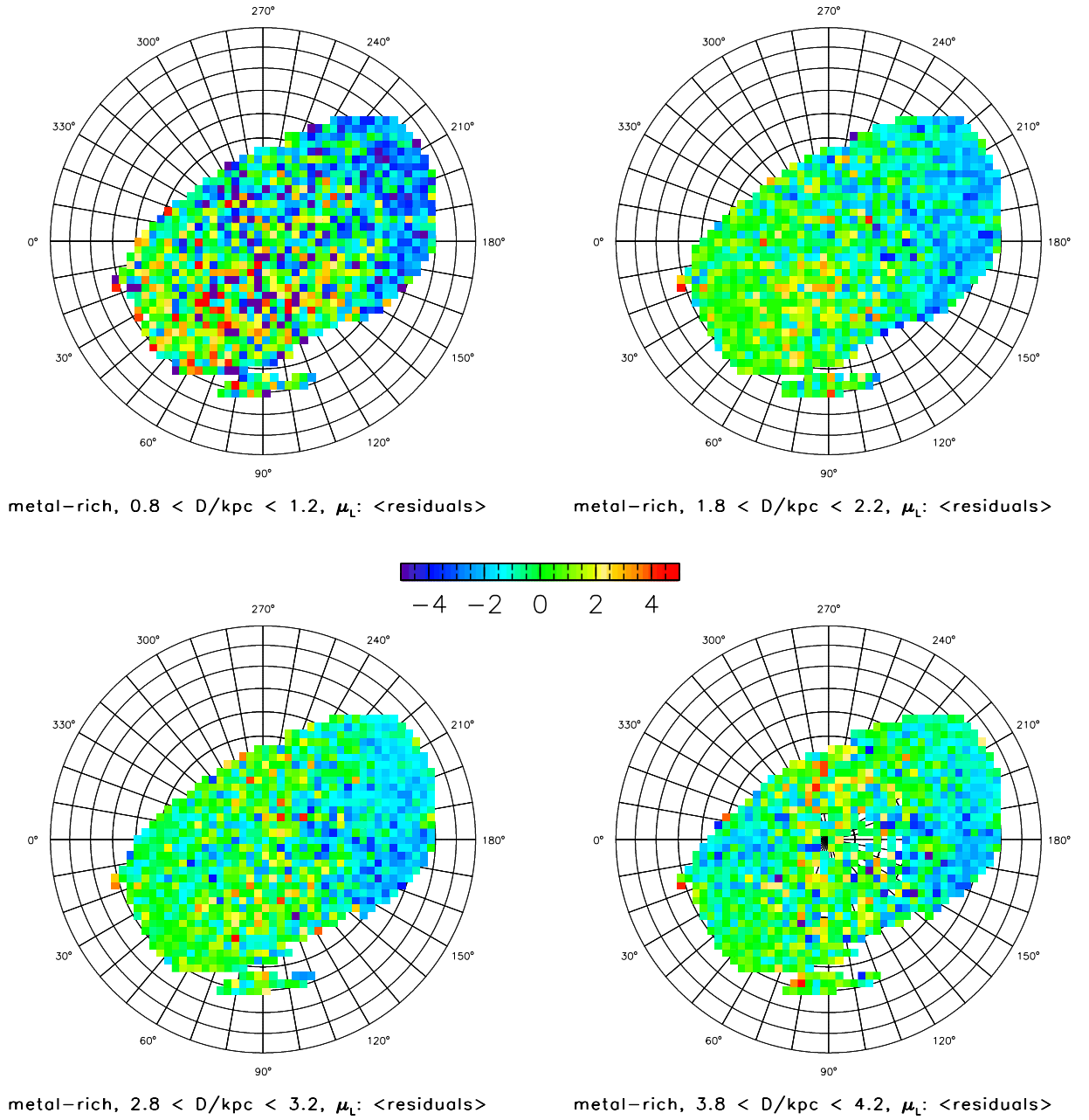FIG. A16.— Analogous to Figure A15, except that the latitudinal proper motion component is shown.

metal−rich, 0.8 < D/kpc < 1.2, μ_L: <residuals>

metal−rich, 1.8 < D/kpc < 2.2, μ_L: <residuals>

metal−rich, 2.8 < D/kpc < 3.2, μ_L: <residuals>

metal−rich, 3.8 < D/kpc < 4.2, μ_L: <residuals>

FIG. A17.— Similar to Figure A15, except that the median difference between the observed value of longitudinal proper motion component and a value predicted by model described in text is shown. All maps are color-coded using the same scale, shown in the middle. Note that the displayed scale is streched by a factor of two compared to the scale from Figure A17, in order to emphasize discrepancies.
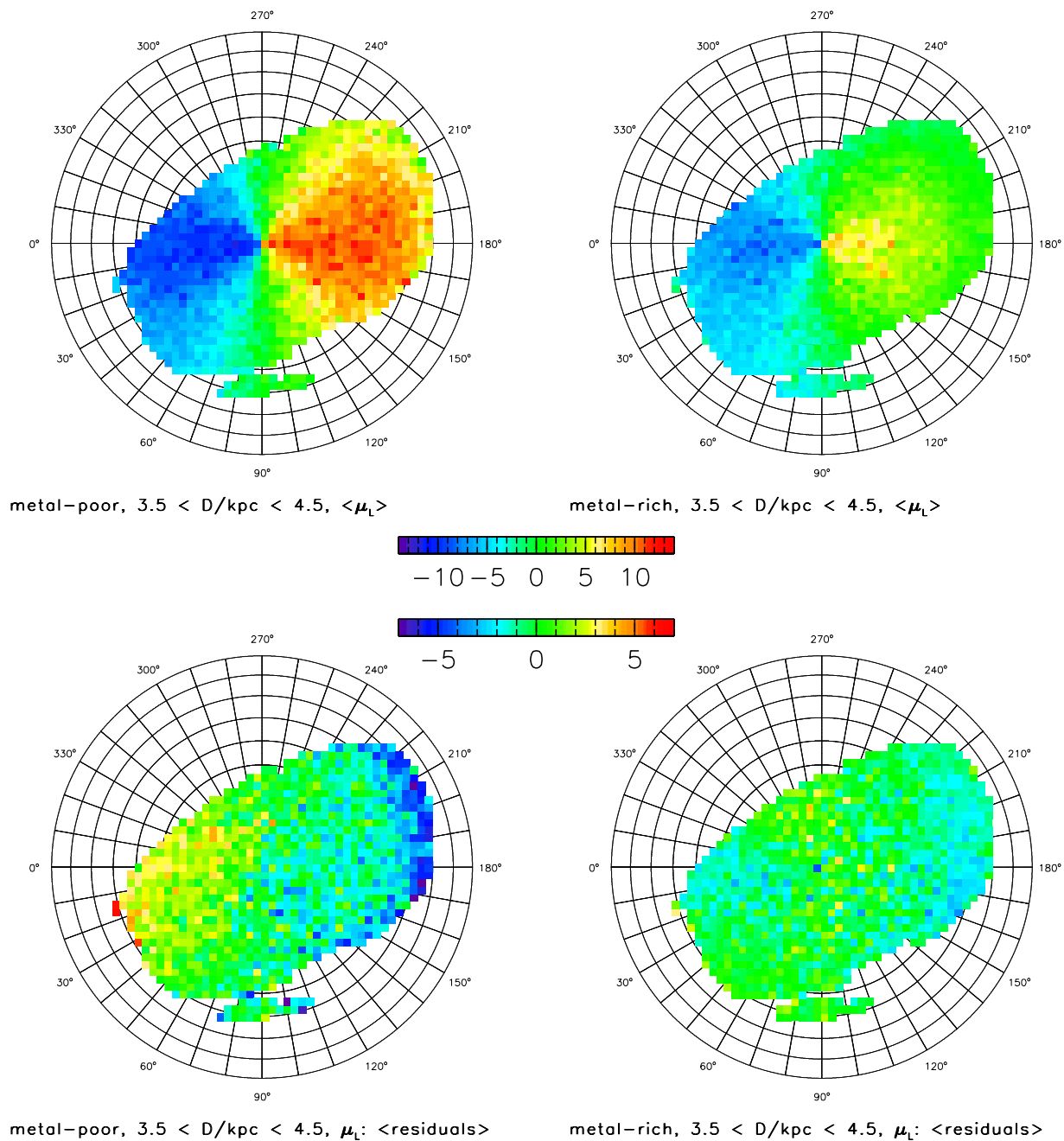
FIG. A18.— Similar to Figures A15 and A17, except that the behavior of high-metallicity (left) and low-metallicity (right) stars is compared in a single distance bin (3.5–4.5 kpc). The top two panels show the median longitudinal proper motion component, and the two bottom panels show the median difference between the observed and model-predicted values. An analogous figure for latitudinal proper motion component has similar characteristics.
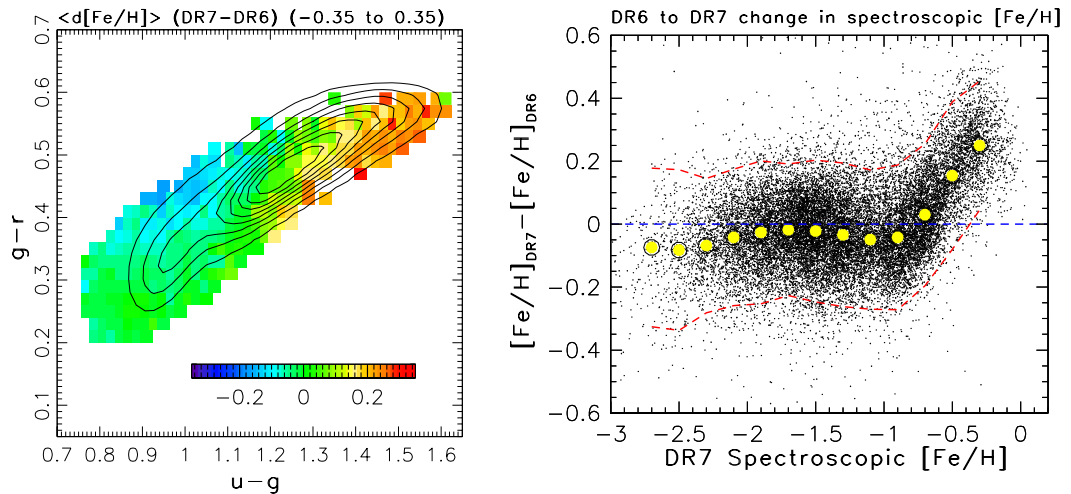
FIG. A19.— A summary of the differences in SDSS spectroscopic metallicity values distributed with Data Releases 6 and 7. The left panel shows the median difference between the DR7 and DR6 values for 0.02×0.02 mag^2 large bins in the $g-r$ vs. $u-g$ color-color diagram, color-coded according to the legend shown in the panel. The largest differences of 0.2-0.3 dex are seen in the top right corner, which corresponds to high metallicities. The right panel shows the difference in metallicities as a function of the new DR7 values. Individual stars are shown by small dots, and the median values of the difference are shown by large circles. The two dashed lines are $\pm 2\sigma$ envelope around these medians, where σ is the root-mean-square scatter (~ 0.1 dex, due to software updates) estimated from the interquartile range. The median differences are larger than 0.1 dex only at the high-metallicity end ($[Fe/H] > -0.6$).
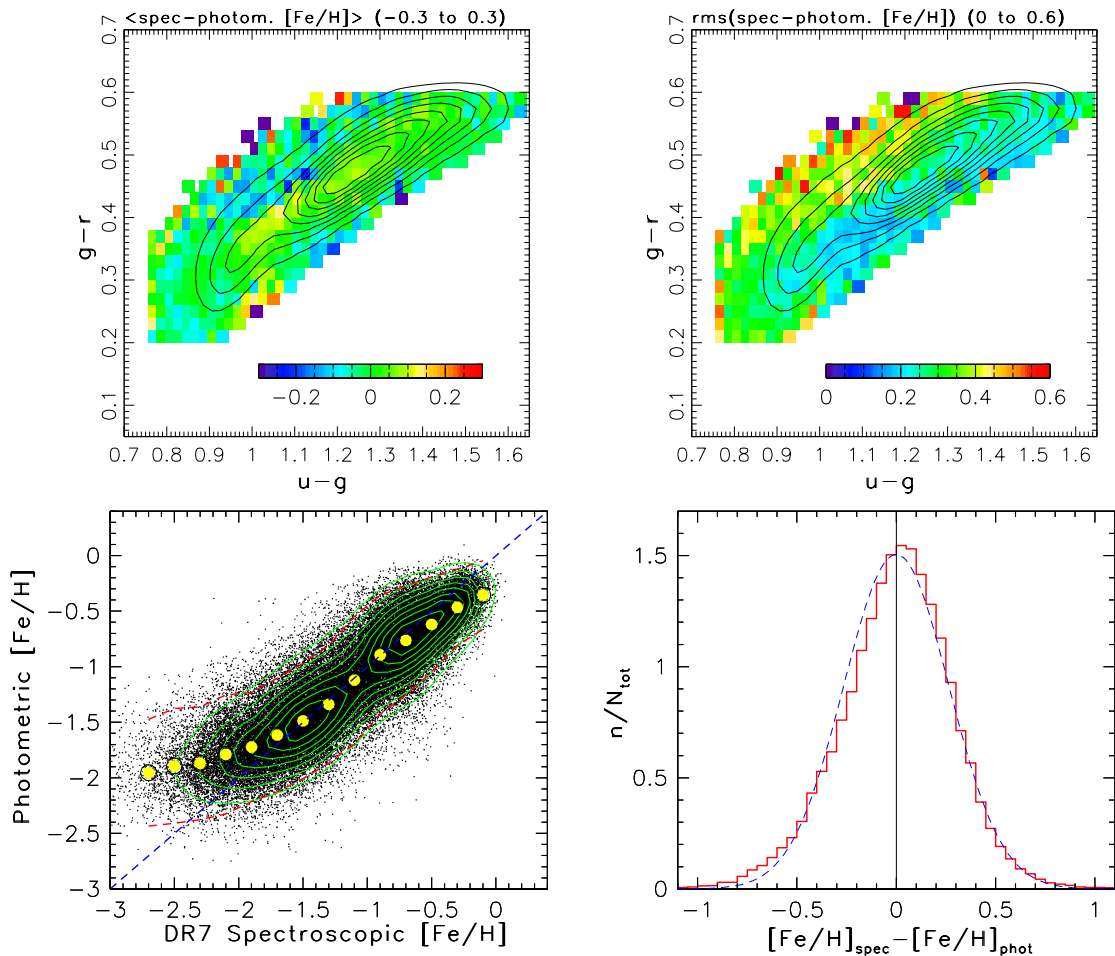
FIG. A20.— The color-coded map in the top left panel shows the median difference between spectroscopic and revised photometric metallicities for ~50,000 stars from SDSS Data Release 7. The median value is zero and the root-mean-square scatter is 0.07 dex. The contours show the distribution of stars with $r < 20$ and at high Galactic latitudes. The top right panel shows the root-mean-square scatter of the difference between spectroscopic and photometric metallicities in each pixel. The top two panels are analogous to the bottom two panels in Figure 2 from I08. The bottom left panel shows the photometric metallicity as a function of the spectroscopic metallicity. Individual stars are shown by small dots, and the median values of the difference are shown by large circles. The distribution of stars is shown as linearly spaced contours. Note that the photometric metallicity saturates at $[Fe/H] \sim -2$ at the low-metallicity end. The histogram in the bottom right panel shows the distribution of the difference between spectroscopic and photometric metallicities for stars with spectroscopic $[Fe/H] > -2.2$. A best-fit Gaussian centered on zero and with a width of 0.26 dex is shown by the dashed line.
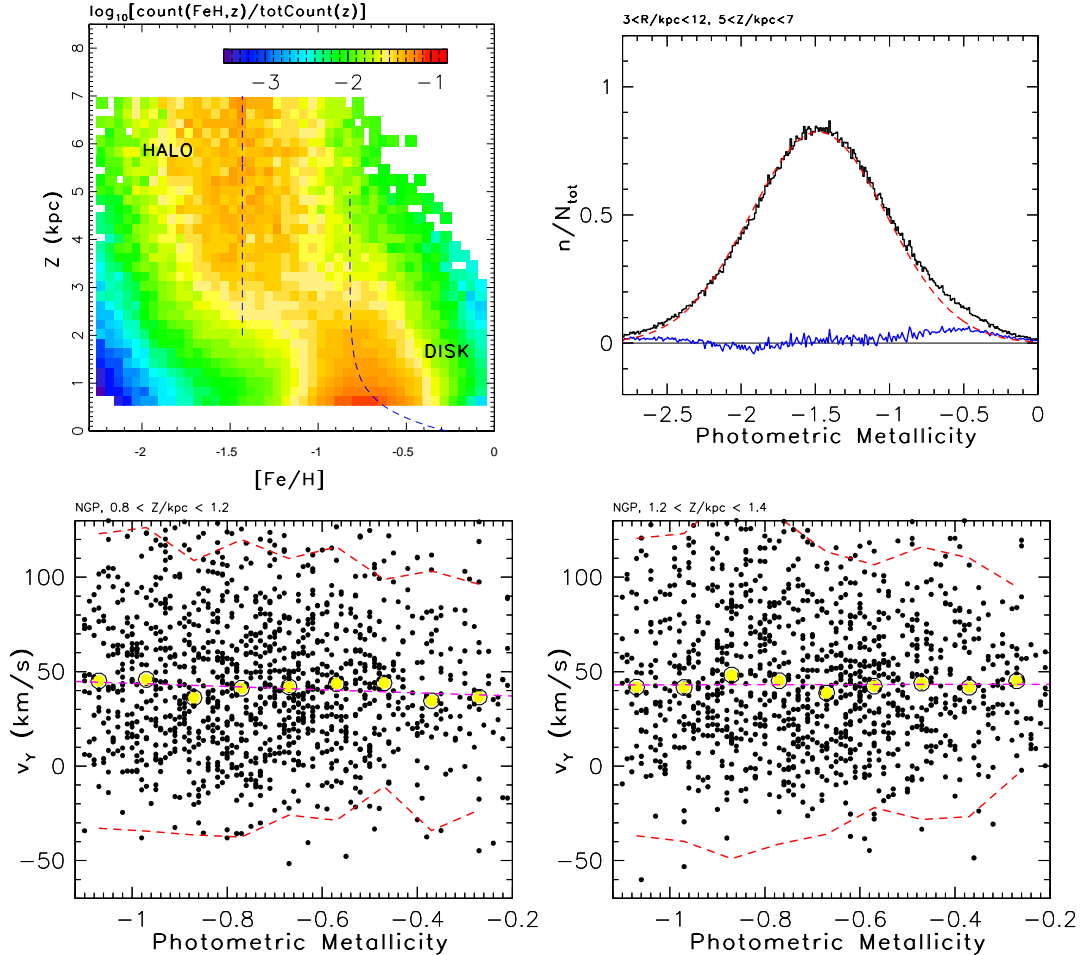
FIG. A21.— The top left panel shows the conditional metallicity distribution as a function of distance from the Galactic plane, and is analogous to the bottom left panel in Figure 9 from I08. Note that the new photometric metallicities include $[Fe/H] > -0.4$. The dashed line which shows the median disk metallicity is also revised (see text). The top right panel is analogous to Figure 10 from I08 and shows the metallicity distribution for stars with 5 kpc $< Z <$ 7 kpc, where Z is the distance from the Galactic plane. Note that the photometric metallicity artifact at $[Fe/H] = -0.5$ discussed by I08 is not present any more. However, there is still evidence, albeit weaker, that disk stars exist at such large distances from the plane (about 5% of stars at such Z are presumably disk stars, in agreement with extrapolation of the exponential profile for counts of disk stars). The bottom two panels show the heliocentric rotational velocity for disk stars in two thin Z slices, and are analogous to the bottom right panel in Figure 16 from I08. Note that the correlation between velocity and metallicity is still absent.
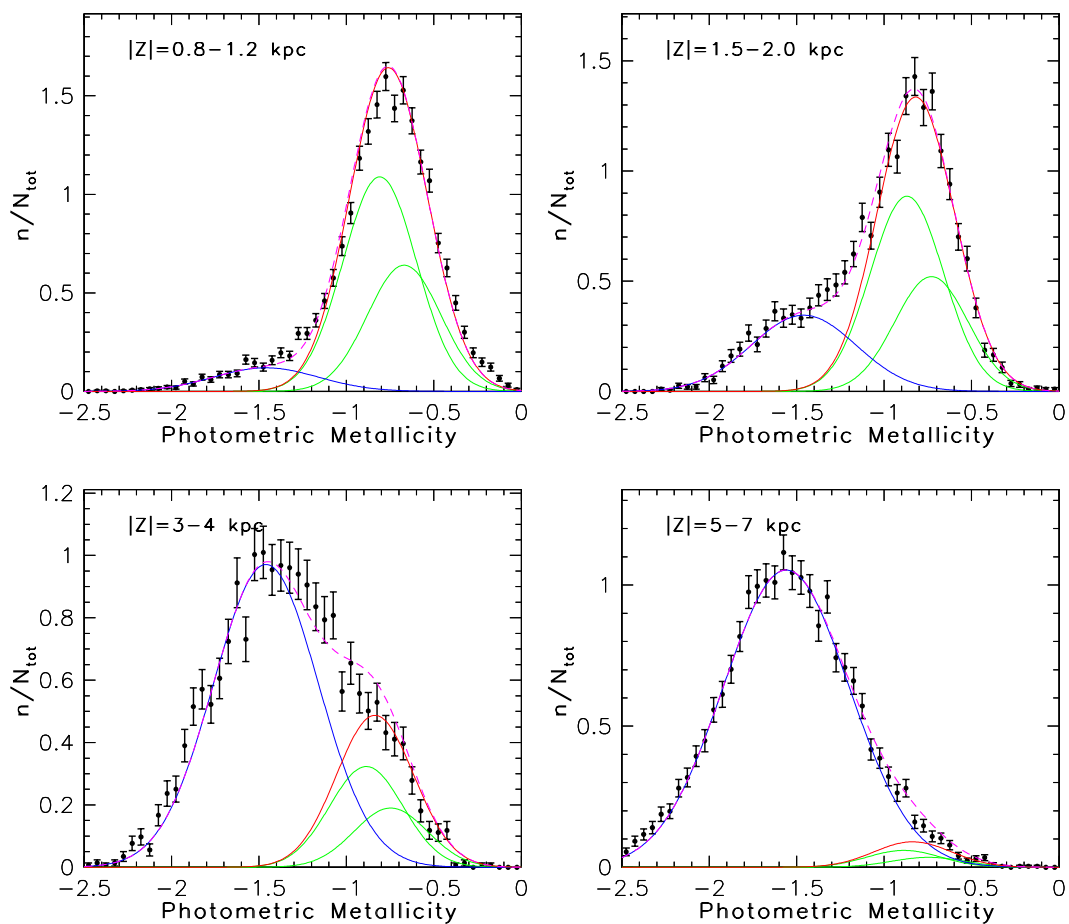
FIG. A22.— Analogous to Figure 7 from I08. The symbols with error bars show metallicity distribution for stars with $0.2 < g-r < 0.4$, 7 kpc $< R <$ 9 kpc and the distances from the galactic plane as marked, where R is the galactic cylindrical radius. The behavior is qualitatively the same as that discussed by I08. The only significant quantitative difference is in the model for the metallicity distribution of disk stars (see text).